Chapter 7: **SPECTROSCOPIC CHARACTERISATION OF THE ACTIVE ION**

The trivalent lanthanide ions have unique spectroscopic properties that are determined by their special electronic structure.[224] The most attractive feature of the optical properties of rare earth ions in crystals is the sharpness of the lines in their absorption and emission spectra. Since the 4*f* shell is efficiently shielded by the closed 5*s* and 5*p* shells, the ligand environment has only a weak influence on the electronic cloud of the lanthanide ions. Therefore, they largely behave like free ions. From the spectra of the lanthanide ions, we can extract information about the electronic structure of the 4*f* shell (described by the position of the peak), the symmetry of the structural position of the lanthanide and the shape of the coordination polyhedron (described by the splitting caused by the crystal field), and the interaction between the lanthanide and its environment (described by the intensity of the spectral lines).[225] A detailed spectroscopic study is then needed to obtain an accurate scheme of the energy level positions and determine the optical behaviour of the system.

7.1. An introduction to the spectroscopy of lanthanide ions.

The energy levels of an ion in a solid matrix are determined by the Hamiltonian that describes the energy states and that takes de following form:

$$H = H_0 + H_{CC} + H_V \qquad \text{Eq. 7.1}$$

where H_0 is the free ion Hamiltonian which includes the kinetics energy, the electrostatic interaction with the nucleus, the electron-electron interaction and the spin-orbit interaction. H_{CC} is the crystal field Hamiltonian which represents the electric field created by the framework. Finally, H_V represents the vibrational interaction.

The free ion Hamiltonian, that describes the electronic structure of a trivalent rare earth ion, has the general form:[226]

$$H_o = h_o + V_{corr} + V_{so} \qquad \text{Eq. 7.2}$$

where H_o is the unperturbed Hamiltonian, h_o is the central field approximation where the basic idea is that each electron is affected by the effective potential created by the atomic nucleus and the rest of the electrons, the operator V_{corr} represents the electron correlation effects and the operator V_{SO} represents the spin-orbit interaction.

The central field approximation can be solved in the Hartree-Fock model and takes the following form:

$$h_o = \sum_{i=1}^{q} \left[-\frac{\hbar^2}{2m_e} \nabla_i^2 + U(r_i) \right] \qquad \text{Eq. 7.3}$$

The contribution by the electrons of a closed shell is considered to be null and the sum is extended to all the electrons of the $4f^n$ configuration. The first part of this equation represents the kinetic energy of the system, where $\hbar$ is $h/2\pi$, and h is the Plank constant and m_e the electron mass. The second term represents the Hartree-Fock potential which, as a scalar operator, is associated with the zeroth-order spherical tensor $U(r_i)$, which represents the potential energy of an electron i as a function of its position (r_i) in the electrical field created by the nucleus. The eigensolutions of the Hamiltonian h_o which can be solved by the Hartree-Fock approximation, can be described as Slater integrals:

$$\psi_{nlm_l m_s}(r) = \frac{1}{r} R_{nl}(r) Y_{lm_l}(\theta,\phi)\chi_{m_s} \qquad \text{Eq. 7.4}$$

where n is the principal quantum number (n = 4 for the 4f electrons), l is the orbital angular momentum (l=3), m_l is the z component of the orbital angular momentum, m_s is the z component of the spin angular momentum, R_{nl} are the radial functions (with n-l-1 nodes), Y_{lm_l} are the spherical harmonics in spherical coordinates, and χ_{m_s} is the spin component. These eigensolutions must respect the exclusion principium of Pauli, and the eigenvalue of the interchange operator (γ) is introduced as a quantum number. In order to have wavefunctions of opposite parity, this operator can only take the value of (–1).

These functions are degenerated, but this degeneration is broken when we consider the non-central part of the Coulomb interaction (V_{corr}), which have the following form:

$$V_{corr} = \sum_{i<j=1}^{N} \frac{e^2}{4\pi\varepsilon_0 r_{ij}} - \sum_{i=1}^{N}\left(\frac{Ze^2}{4\pi\varepsilon_0 r_i} - V(r_i)\right) \qquad \text{Eq. 7.5}$$

where $V(r_i)$ is the self-consistent potential. This term gives us the total angular orbital momentum (L) and the spin angular momentum (S), splitting the energy levels in terms ^{2S+1}L with a typical energetic separation of around 10^4 cm^{-1}.

The spin-orbit interaction operator has the following form:

$$V_{so} = \zeta \sum_{i=1}^{q} s_i \cdot l_i \qquad \text{Eq. 7.6}$$

where ζ is the spin-orbit coupling constant, and s_i and l_i are the spin and the orbital angular momenta for each electron. The spin-orbit interaction, of magnetic origin, provides the total angular momentum (J), defined as $J = L+S$, splitting the different electronic terms in levels $^{2S+1}L_J$ with a typical energetic separation of around 10^3 cm^{-1}.

This process by which the electronic levels $^{2S+1}L_J$ are formed is known as Rusell-Saunders coupling or L-S coupling. This coupling can be used when the spin-orbit interaction is small compared with the non-central part of the Coulomb interaction.

As the atomic number increases, the mean speed of the electrons increases with the relativistic effects due to the spin-orbit interaction. In atoms whose atomic number is high, the spin-orbit interaction becomes higher than the interelectronic repulsion energy, and we must consider V_{so} in the

Hamiltonian before V_{corr}. In this way, the orbital and the spin angular momenta of each electron are combined to obtain a total angular momentum j_i for each electron. These j_i are then combined to obtain the total angular momentum J. This is j-j mixing.

In heavy atoms, as in the case of lanthanides, the reality is that the non-central part of the Coulomb interaction and the spin-orbit interaction can be considered to be of the same order. These interactions can be understood as perturbations to the degenerated levels of the $4f^n$ configuration. In this, the Russell-Saunders coupling is not valid, and we must describe the energetic terms as a combination of the various Russell-Saunders terms.[227]

The crystal field interacts with the active ion as an external electrical field: a perturbation on the electrons of the central lanthanide ion caused by the surrounding ligands represented by the crystal field potential (V_{CC}). This causes the energetic levels to split into Stark sublevels $^{2S+1}L_J(M_J)$, and at the same time induces the oscillator strengths in the transition.[228,229] This V_{CC} can be treated as a perturbation. This means that the matrix, which contains the elements of h_o, V_{corr} and V_{so}, is diagonalised, while the crystal field effect is taken into account by adding to the energy the corrections which are evaluated with the free ionic system wavefunctions in the way defined by the standard perturbation theory. The most common expression for describing the crystal field operator in the literature is:

$$V_{CC} = \sum_{k,t} B_k^t \sum_i C_t^{(k)}(r_i) \qquad \text{Eq. 7.7}$$

where B_t^k are the crystal field parameters that represent the symmetry of the system and $C_t^{(k)}$ is the spherical tensor operator.

In practice, the sums in equation 7.6 are limited in the $4f$ systems to $k = 7$. Also, this potential can be divided into two parts: one with even k (responsible for the splitting caused by the crystal field) and one with odd k (mainly responsible for the intensity of the electric dipolar transitions).

The crystal field breaks the $2J+1$ degeneracy of the levels of the free ion and mixes the states, thus changing the gravity centre of the multiplet $^{2S+1}L_J$. However, because the external electrons are shielded, this shifting is small with to respect the gravity centre of the free ion. Every level degenerated $2J+1$ times is split into sublevels, thus generating $2J+1$ Stark sublevels. Finally, the real number of Stark sublevels will depend on the symmetry of the crystal field and the value of J. When J is an integer, there are $2J+1$ sublevels and when J is a semi-integer, there are $(2J+1)/2$ Kramers degenerated doublets.

The optical absorption of lanthanides is due to 4*f*-4*f* intraconfigurational transitions. The probability of transition between two electronic states, *i* (initial state) and *f* (final state), of an intraconfigurational transition, is given by the matrix element

$$\langle f, n | H_1 | i, n' \rangle \qquad \text{Eq. 7.8}$$

where H_1 is the Hamiltonian that represents the interaction between the electromagnetic field of the incident light and the electrons of the lanthanide, and *n* and *n'* are the creation and annihilation operators. This Hamiltonian is represented by its potential vector $A \approx e^{\pm i\vec{k}\vec{r}}$, and the electric dipolar moment $\vec{p}$, and takes the following form:

$$H_1 = \sum \frac{e}{m_e c} \vec{A} \cdot \vec{p} \qquad \text{Eq. 7.9}$$

where *c* is the speed of light. The sum is extended to all the electrons that participate in the interaction.

The product $e^{\pm i\vec{k}\vec{r}} \cdot \vec{p}$ can be developed in three sums. The first one is proportional to $e\vec{r}_i$ (electric dipolar transitions), the second is proportional to $\vec{l}_k \times \vec{L}$ (magnetic dipolar transitions), and the third is proportional to $(\vec{k} \cdot \vec{r}) \cdot \vec{r}$ (electric quadripolar transitions).[225,230,231]

The electric dipolar transitions cause most of the narrow lines in the spectra of the lanthanides. The creation of an electric dipole is the result of a linear shifting of the electronic charge. This dipole then changes the orientation of its charge under an inversion centre, having an even parity. In lanthanide ions, the electric dipolar transitions are forbidden by parity (Laporte's rule) and wavefunctions of opposite parity must be mixed. These transitions are therefore forced or induced, and several mechanisms, involving interactions with vibrations of the crystal structure, have been presented to explain why these transitions are allowed. The dichroic behaviour of the optical transitions is given by the selection rules between levels with the same or different irreducible representation.

The magnetic dipolar transitions are caused, via a magnetic dipole mechanism, by the interaction between the active ion and the magnetic field of the light. This magnetic dipole may be considered as a rotational shifting of the electronic charge, and as the direction of rotation is not changed by an inversion centre, it has an odd parity. Therefore, the dipolar magnetic transitions are formally allowed in the lanthanides. However, we will not consider these kinds of transitions because the lanthanides used in this Thesis do not have pure magnetic dipolar transitions.

The electric quadripolar transitions are caused by an electric quadripole, the parity of which is always odd, so the quadripolar electric transitions between different $4f^n$ states are allowed.

In 1962, Judd[232] observed that some transitions in the lanthanides were sensitive to the solvent used. These transitions followed the selection rules of the quadripolar electric transitions, which is why they are also called pseudo-quadripolar transitions or hypersensitive transitions. The intensity of these transitions is generally the highest in the 4*f*-4*f* transitions of a lanthanide.

7.2. Optical properties of Er^{3+} in $RbTiOPO_4$:Nb crystals.

Typically, the samples of RTP:Nb doped with Er^{3+} are pink, mainly because of the absorption of the hypersensitive transition $^4I_{15/2} \rightarrow {}^2H_{11/2}$ near 530 nm, with a green spectral colour and an unsaturated red or pink complementary colour.[232] The other hypersensitive transition of this ion ($^4I_{15/2} \rightarrow {}^4G_{11/2}$) is in the ultraviolet region, but this has no implications for the colour of the sample. Er^{3+} has five metastables states, which means that the transitions from these states can be used in laser studies. These states are $^2H_{9/2}$, $^4S_{3/2}$, $^4F_{9/2}$, $^4I_{11/2}$, $^4I_{13/2}$.[233]

The spectra obtained in this section were measured using polarised light parallel to the three crystallographic axes of the crystal at room temperature because they coincided with the three principal optical axes with the following correlation ***a*** = *x*, ***b*** = *y* and ***c*** = *z*. Any measurement taken out of these directions will produce a composition of the optical absorption in the three principal axes.

7.2.1. Optical absorption of Er^{3+}.

The $4f^{11}$ configuration of Er^{3+} gives 17 multiplet terms. Placing the active ion in a low symmetry place, can, due to spin-orbit coupling, lead to 41 levels.[220] In RTP:Nb as-grown crystals, as in RTP and KTP,[121] the multiplets lying at an energy above 20000 cm^{-1} (500 nm) overlap with a background absorption due to point defects of the lattice[209,211] (see Chapter 6). To minimise this absorption, the samples were heated for 3 h to 773 K before the measurements were taken. Also, the residual background absorption was analytically evaluated in the side regions of each multiplet and discounted of the spectra measured.

Figure 8 in *paper V* shows the room-temperature (RT) unpolarised optical absorption spectra of Er^{3+} in $RbTi_{0.967}Nb_{0.026}Er_{0.007}OPO_4$. The band sets are labelled according to the energy level diagram of erbium, whose average positions are not very sensitive to the host.[234] Eleven multiplets were clearly resolved. These were $^4G_{9/2}$, $^4G_{11/2}$, $^2H_{9/2}$, $^4F_{3/2}$, $^4F_{5/2}$, $^4F_{7/2}$, $^2H_{11/2}$, $^4S_{3/2}$, $^4F_{9/2}$, $^4I_{11/2}$ and $^4I_{13/2}$. The $^4I_{9/2}$ manifold was identified but could not be resolved because of its low intensity. As the Er concentration

in this sample (0.65×10^{20} ions·cm^{-3}) was higher than the one obtained in KTP and RTP (see *paper I*), the spectrum was better defined and more intense.

Also, polarised optical absorption spectra were recorded parallel to the three crystallographic axes. The results are shown in Figure 7.1. Part of these spectra were shown previously in Figure 4 in *paper II* and in Figures 5 and 6 in *paper VI*, which contains a detailed description of them. The optical absorption cross-section in the 1450-1650 nm region was 8.57×10^{-21} cm^2 at 1541.5 nm (6487 cm^{-1}) for polarisation parallel to the ***c*** crystallographic axis. This absorption cross-section was the highest ever obtained for Er^{3+} in a crystal of the KTP family.

We studied the optical absorption at 6 K to determine the sublevels of all the possible excited energy levels caused by the elimination of the thermal lattice vibrations. We assumed that at this temperature, only the lowest sublevel of the $^4I_{15/2}$ was populated, and this produced narrow and intense optical absorption bands corresponding to transitions from the fundamental Stark sublevel of this multiplet to the sublevels of the excited multiplets. The number of sublevels arising from the interaction with the crystal field of the lattice with different energy depends on the symmetry of the crystal field. For Er^{3+} in this matrix, the maximum number of sublevels expected for each multiplet is $(2J+1)/2$, because of the Kramers degeneracy of its odd $4f^{11}$ electron configuration and the low symmetry where erbium is located (C_1). The shape of the absorption lines should therefore reflect the transition probabilities from the lowest sublevel of the ground level to the sublevels of each excited energy level of erbium. Figure 7.2 shows the spectra, recorded with light polarised parallel to the three crystallographic axes. Part of these spectra were shown in Figure 4 in *paper II*, Figure 3 in *paper IV* and Figure 2 in *paper IX*. The signal at 6 K was much more intense than the signals at RT. This was because at 6 K all the electronic population was in the lowest sublevel of the ground energy level. In this way, at 6 K, almost all the energy was concentrated in only one transition and this was more intense than at RT, where the energy was distributed between several transitions, starting from the different energy sublevels of the ground energy level. We must point out the exception of the $^4I_{13/2}$ multiplet (see *paper II*) where the intensities of the various polarisations were similar. At this temperature we were able to resolve the $^2K_{15/2}$ multiplet. Because erbium has an odd number of electrons in the $4f$ shell, no selection rules are expected for the polarisation of the electronic transitions. This means that for erbium the number of peaks and their energy position do not depend on the polarisation of the incident light, but intensity variation of the peaks associated with the three polarisations is still possible, as was confirmed experimentally both in the spectra recorded at RT and in the spectra recorded at 6 K. Using such dichroic material will support the advantages for obtaining polarised laser emissions.

Table 7.1 gives the energy positions of the absorption bands for each multiplet. With only small changes, the positions of the Er^{3+} bands were similar to those in RTP and KTP lattices. In many

multiplets, the number of peaks experimentally observed was larger than the maximum number of sublevels expected for a single erbium centre. Indeed, if no thermally induced anti-Stokes transitions occur and if the angular momentum J is a good quantum number, the number of lines within one type of centre is expected to be $J + ½$. Particularly in the $^4G_{11/2}$, $^2H_{11/2}$, $^4S_{3/2}$ and $^4F_{9/2}$ manifolds, we observe at least twice as many lines as are expected with J = 11/2, 3/2 and 9/2, respectively. Figure 2 in *paper IX* and the subsequent discussion prove that there are more than one site for Er in RTP:(Nb,Er) lattice. The hypothesis of two sites for Er in this crystal would agree with the occupancy of the two inequivalent titanium sites of the lattice, as deduced from the results of neutron powder diffraction in RTP:(Nb,Er) crystals (see Chapter 4). These results can be qualitatively understood if we assume that the Ti(2) site is more populated than the Ti(1) site (see Chapter 4). In this way, only the centre with the lowest population contributes to the absorption spectrum parallel to the ***a***-axis. The centre with the highest population mainly contributes to the absorption parallel to the ***b***-axis, and both centres contribute to the absorption parallel to the ***c***-axis.

Table 7.1. *Splitting of the excited energy levels of Er^{3+} in RTP:Nb obtained at 6 K.*

$^{2S+1}L_J$	Position (nm/cm^{-1})		
$^2K_{15/2}$		357.9 (27941)	
		358.3 (27909)	
		359.2 (27839)	
		359.4 (27824)	
		361.2 (27685)	
		361.4 (27670)	
$^4G_{9/2}$	365.0 (27397)		
	365.4 (27367)		
	366.2 (27307)		
	366.6 (27278)		
	367.4 (27218)		
			371.8 (26896)
			372.1 (26872)
			372.3 (26860)
			372.7 (26831)
			373.0 (26810)

$^4G_{11/2}$	376.5 (26560)			
	376.9 (26532)			
	377.4 (26497)			
	377.8 (26469)			
	378.0 (26455)			
	378.3 (26434)			
		380.7 (26267)		
		380.8 (26260)		
		381.1 (26240)		
		381.4 (26219)		
		382.3 (26157)		
		382.5 (26144)		
			382.9 (26116)	
			383.0 (26110)	
			383.3 (26089)	
			383.5 (26076)	
			383.8 (26055)	
			384.4 (26014)	
$^2H_{9/2}$	405.8 (24643)			
			406.1 (24624)	
	406.7 (24588)			
			407.0 (24570)	
	407.8 (24522)			
			408.1 (24504)	
	408.7 (24468)			
			409.0 (24450)	
	409.6 (24414)			
			409.9 (24396)	
$^4F_{3/2}$		443.0 (22573)		
		444.6 (22492)		
$^4F_{5/2}$	449.5 (22247)			
			450.0 (22222)	
	451.9 (22129)			
	452.2 (22114)			
			452.5 (22099)	
$^4F_{7/2}$	485.5 (20597)			
			485.9 (20580)	
	487.7 (20504)			
			488.3 (20479)	
	489.7 (20421)			
			490.0 (20408)	
	491.0 (20366)			
			491.4 (20350)	
$^2H_{11/2}$		518.0 (19305)		
	518.2 (19297)			
		518.5 (19286)		
	518.7 (19279)			
	519.2 (19260)			
		519.5 (19249)		
	519.9 (19234)			
	520.4 (19216)			
	521.0 (19194)			
		521.4 (19179)		
			522.6 (19135)	
			523.2 (19113)	
			523.7 (19095)	
			524.1 (19080)	
			524.2 (19077)	
			524.5 (19066)	
$^4S_{3/2}$			546.1 (18312)	

				546.4 (18302)
	547.3 (18271)			
		547.9 (18251)		
				548.2 (18241)
	548.6 (18228)			
		549.3 (18205)		
$^4F_{9/2}$	645.6 (15489)			
			646.4 (15470)	
	650.8 (15366)			
			651.2 (15356)	
	652.3 (15330)			
			653.4 (15304)	
	657.7 (15204)			
			658.4 (15188)	
	659.4 (15165)			
			659.9 (15154)	
$^4I_{9/2}$	790.9 (12644)			
	792.6 (12617)			
	794.2 (12591)			
	796.1 (12561)			
	799.4 (12509)			
			804.9 (12424)	
			806.0 (12407)	
			807.3 (12387)	
			809.3 (12356)	
			810.7 (12335)	
$^4I_{11/2}$		965.0 (10363)		
		967.5 (10336)		
		968.5 (10325)		
		969.5 (10314)		
		980.4 (10200)		
		987.0 (10132)		
$^4I_{13/2}$	1518.2 (6587)			
			1518.9 (6584)	
	1523.2 (6565)			
			1523.9 (6562)	
	1528.1 (6544)			
			1528.9 (6541)	
	1532.6 (6525)			
			1533.2 (6522)	
	1535.9 (6511)			
			1536.8 (6507)	
	1539.6 (6495)			
			1539.9 (6494)	
	1541.6 (6487)			
			1542.3 (6484)	

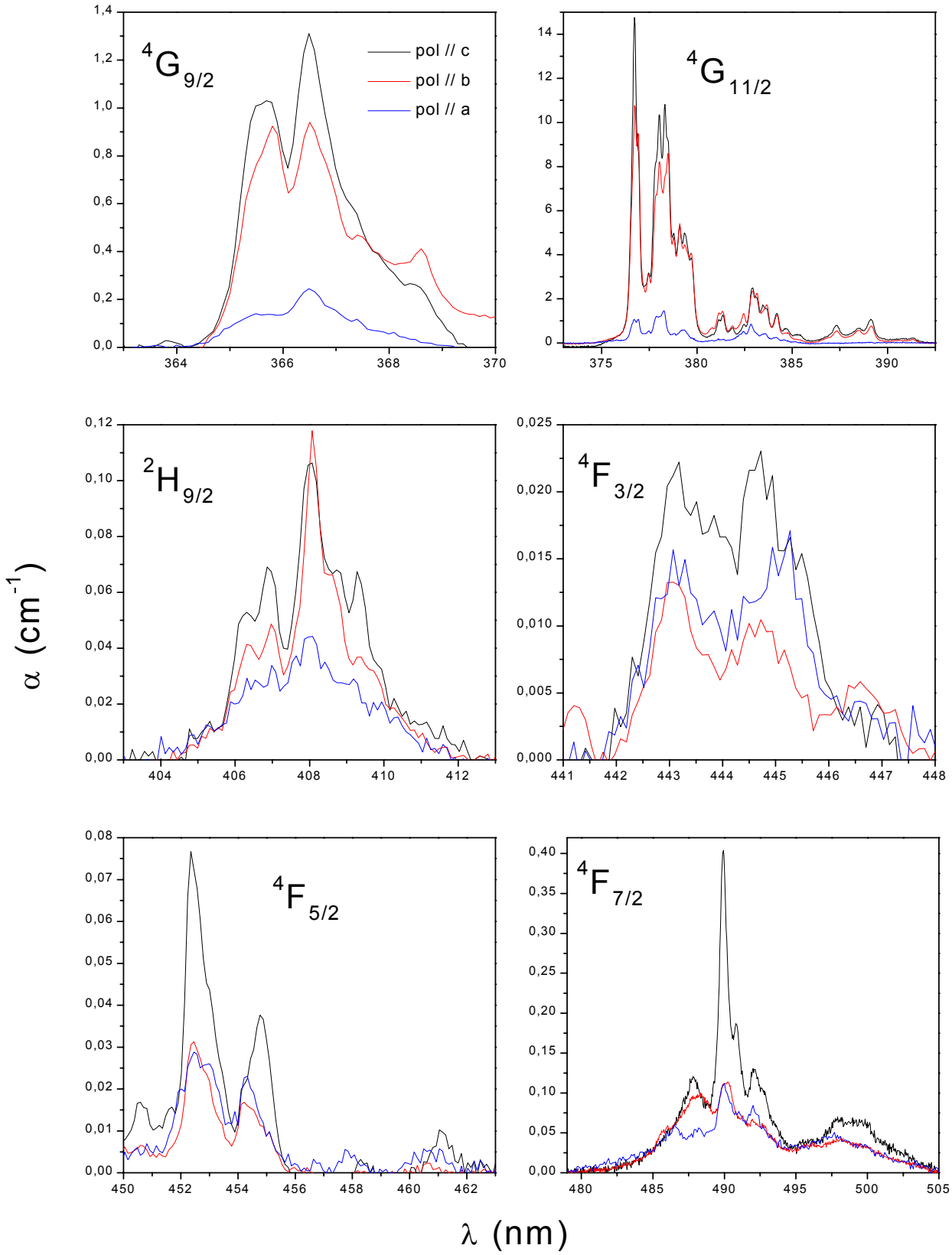

Figure 7.1.(a). *Polarised optical absorption of erbium in RTP:Nb single crystal in the 350-500 nm range at room temperature.*

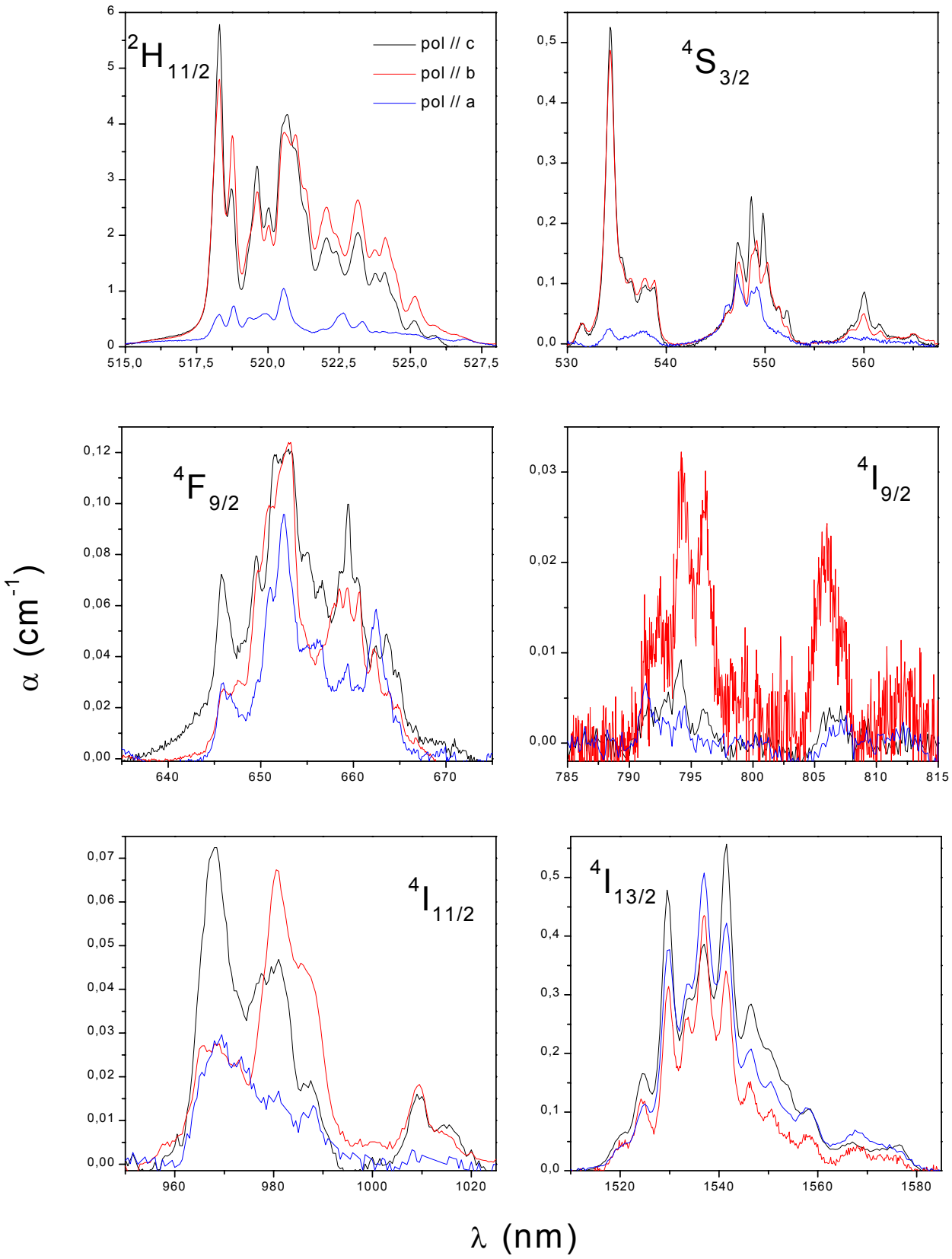

Figure 7.1.(b). *Polarised optical absorption of erbium in RTP:Nb single crystals in the 500-1600 nm range at room temperature.*

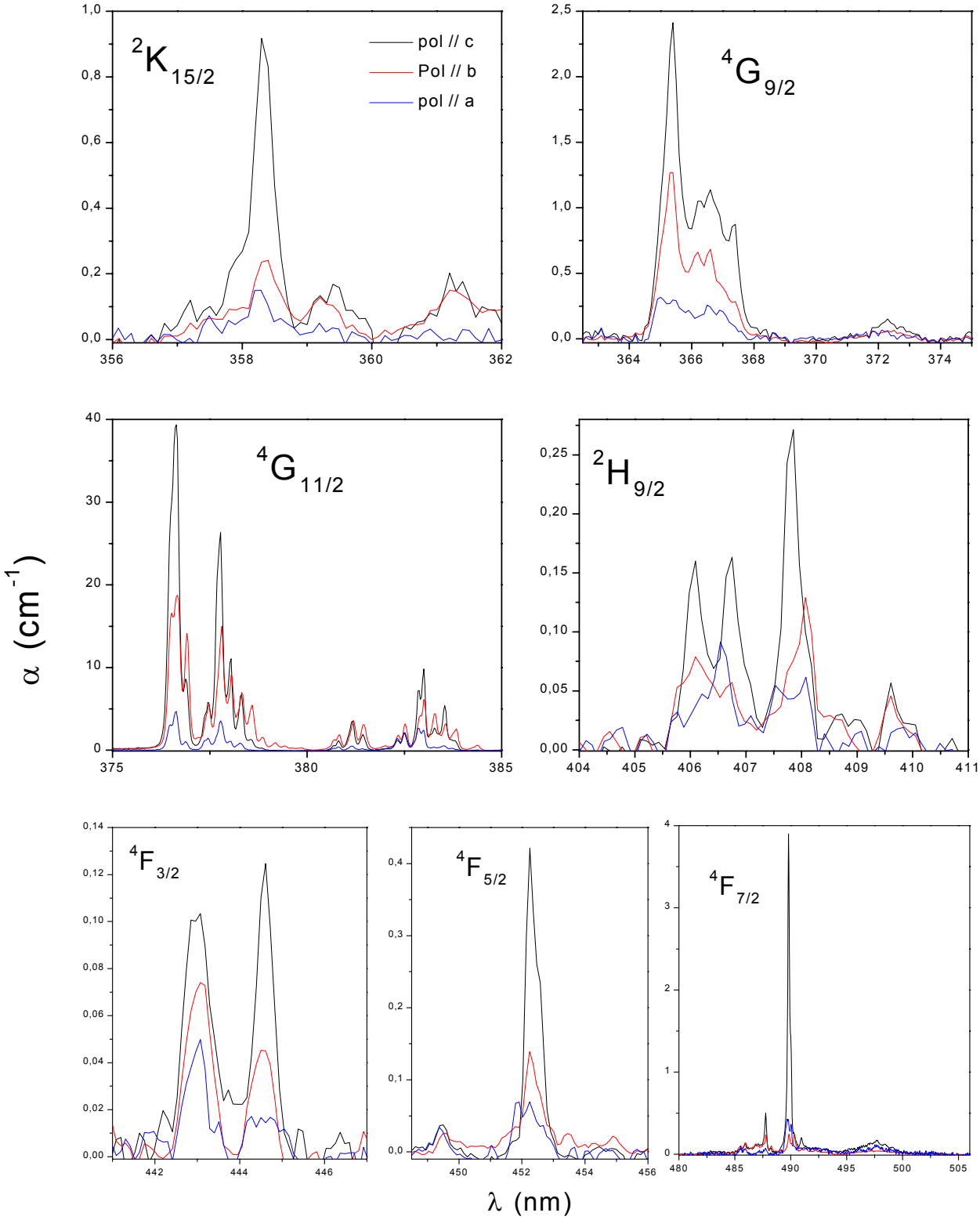

Figure 7.2.(a). *Polarised optical absorption of erbium in RTP:Nb single crystal in the 350-500 nm range at 6 K.*

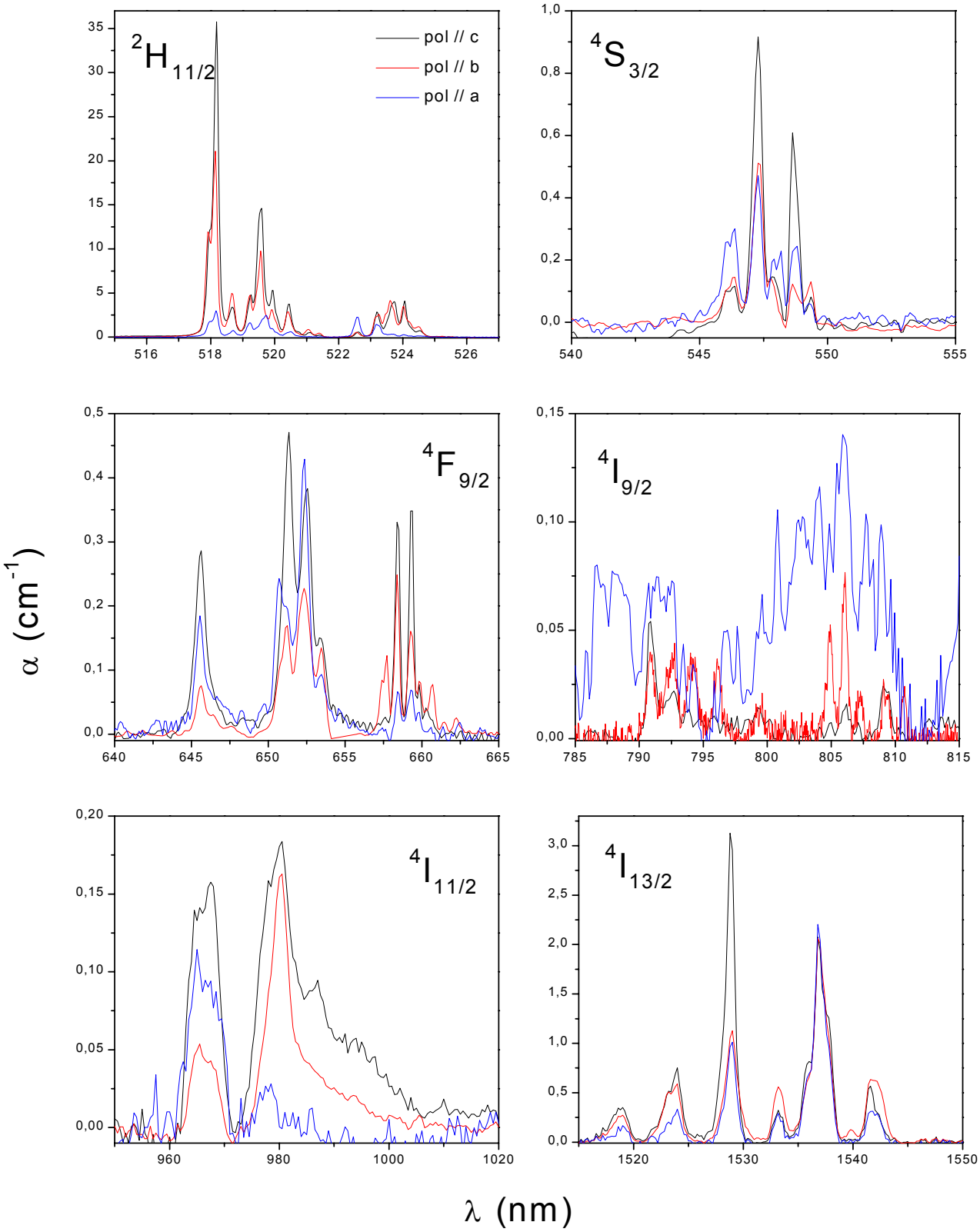

Figure 7.2.(b). *Polarised optical absorption of erbium in RTP:Nb single crystal in the 500-1600 nm range at 6 K.*

7.2.2. Theoretical simulation using the Judd-Ofelt theory.

7.2.2.1. Theoretical background.

The theory by which to calculate the intensity of the intra-configurational radiative electric dipolar transitions in an isotropic material was developed independently by Judd and Ofelt in 1962.[232,235] This theory is based on the approximation of the configuration of the free ion and describes monofononic processes and produces a good correlation between the theoretical numerological model of the *f-f* electronic transitions and the experimental data obtained from the absorption spectroscopy. It is therefore very useful for predicting the parameters of the luminescent radiative transitions. The Judd-Ofelt theory is only valid for the electronic transitions induced by the electric dipolar mechanism.

The probability (P_{if}) that a radiative transition (absorption or emission) between two different levels occurs is given quantically by the following expression:

$$P_{if} = \frac{2\pi}{\hbar}\left|\langle i|H|f\rangle\right| \qquad \text{Eq. 7.10}$$

where $\langle i|$ and $|f\rangle$ represent the initial and final states of the transition, respectively and H corresponds with the Hamiltonian of the interaction, which is responsible for the radiative transition.

The operator of the electric dipolar moment (D) is expressed by:

$$D = -e\sum_i r_i \equiv -eD_t^k \qquad \text{Eq. 7.11}$$

where the sum is extended to all the electrons and e is the electron charge. The position r_i, must be expressed in a tensorial form:

$$D_t^k = \sum_i r_i^k C_t^k(\theta_i, \phi_i) \qquad \text{Eq. 7.12}$$

where D_t^k is a rotational matrix of rank $k = 1$ with t components. These components are the numbers of polarisation and indicate the polarisation of the light. They can take the values $t = 0$ (associated to the z component) and $t = \pm 1$ (associated to the x or y component). $C_t^k(\theta_i, \phi_i)$ is the irreducible tensorial component related to the spherical harmonics (Y_t^k) by the expression:

$$C_t^k = \sqrt{\frac{4\pi}{2k+1}} Y_t^k \qquad \text{Eq. 7.13}$$

Taking into account this expression for the electric dipolar moment and the *i* and *f* states from the $4f^n$ configuration, we obtain states of the same parity. Then, by Laporte's rule, in a first approximation the probability of the radiative transition is null. The solution is to mix the *i* and *f* states from the configurations of opposite-parity to the $4f^n$, as they can be $4f^{n-1}$ n'd^l, $4f^{n-1}$ n'g^l or configurations with $4d^9\ 4f^{n+1}$. Judd and Ofelt believed that the even terms (*k* = even) of the crystal field operator in equation 7.6 were responsible for these mixed configurations with opposite-parity. What happens is that the states of the lanthanides ($\left|4f^n(\gamma SL)JJ_z\right\rangle$) and states of the excited configurations with a different parity $\left|\varphi_{nl}\right\rangle$ mix. If we consider the crystal field as a perturbation of first order, we can obtain the mixed states as follows:

$$\left|A'\right\rangle = \left|4f^N(\gamma SL)JJ_z\right\rangle + \sum_k \frac{\left\langle 4f^N(\gamma SL)JJ_z \middle| V_{cc,odd} \middle| \varphi_{nl}\right\rangle}{E(4f^N J) - E(\varphi_{nl})} \left|\varphi_{nl}\right\rangle \qquad \text{Eq. 7.14}$$

$$\left|B'\right\rangle = \left|4f^N(\gamma' S' L')J'J'_z\right\rangle + \sum_k \frac{\left\langle 4f^N(\gamma' S' L')J'J'_z \middle| V_{cc,odd} \middle| \varphi_{nl}\right\rangle}{E(4f^N J') - E(\varphi_{nl})} \left|\varphi_{nl}\right\rangle \qquad \text{Eq. 7.15}$$

where *k* represents the quantum numbers of the excited configuration and *E* is the energy of the different states.

The oscillator strength ($f_{ED,th}$) of a transition is defined as an adimensional magnitude related directly with the P_{if}:

$$f_{ED,th} = \chi\left[\frac{8\pi^2 mc\sigma}{h}\right]\left|\left\langle A'\middle|D_t^{(1)}\middle|B'\right\rangle\right|^2 \qquad \text{Eq. 7.16}$$

where σ is the energy of the transition and χ is the Lorentz correction, applied to the effective electric field on the active centres in an isotropic medium of refractive index *n* due to the polarisation induced by the matrix.[227] For absorption phenomena due to electric dipolar transitions, this correction is expressed as follows:

$$\chi = \frac{\left(n^2+2\right)^2}{9n} \qquad \text{Eq. 7.17}$$

The line intensity (S_{ED}) is the quadratic term of the oscillator strength. It measures the strength of the electric dipolar transition from the *J* level to the *J'* level. If we use the function that describes the mixed states of the lanthanide ions, the line intensity can be calculated for each transition in a theoretical way, without any experimental measurement:

$$S_{ED}=\left[\sum_{k,t,p} A_{tp}\left\{\frac{\left\langle 4f^N \phi J J_z \middle| D_q^1 \middle| \varphi_{nl}\right\rangle\left\langle \varphi_{nl} \middle| D_p^t \middle| 4f^N \phi' J' J_z'\right\rangle}{E\left(4f^N J'\right)-E\left(\varphi_{nl}\right)}+\frac{\left\langle 4f^N \phi J J_z \middle| D_q^t \middle| \varphi_{nl}\right\rangle\left\langle \varphi_{nl} \middle| D_p^1 \middle| 4f^N \phi' J' J_z'\right\rangle}{E\left(4f^N J\right)-E\left(\varphi_{nl}\right)}\right\}\right]^2 \qquad \text{Eq.7.18}$$

where A_{tp} are the components of the crystal field, $\phi = \gamma SL$ and $\phi' = \gamma' S' L'$. However, we must also take into account the following approximations:

- The excited configurations are considered to be degenerated although the energetic bandgap between the ground state and the first excited configuration (intraconfigurational transitions) in the lanthanides is around 60000-100000 cm^{-1}. This approximation notably simplifies the calculation because sums of over φ_{nl} are possible, and we can apply the *closure* relation to obtain an even tensorial operator for the matrix elements of the tensorial operators ($U_{p+t}^{(\lambda)}$). Although these approximations appear rough, they obtain accurate results.

- We suppose that the energetic bandgaps between states are *J* independent. The energetic bandgap between two states can then be substituted by a constant (ΔE). Like the previous approximation, this also simplifies the calculation, but it is unreal because the transitions between states with a different *J* in the lanthanides are very energetic.

- We suppose that all the Stark levels of the different multiplets have the same electronic population. This approximation is partially true at room temperature, although the Stark splitting of the ground multiplet is of the order of 500 cm^{-1}. However, summing different transitions involving different states tends to reduce the differences between the populations of the different levels.

When we perform these approximations and assume that the material is isotropic, if we eliminate the directional dependencies on t, S_{ED} can be expressed as a sum of the product of three phenomenological parameters Ω_λ (the Judd-Ofelt parameters) and the reduced matrix elements of the tensorial operators U^{λ}_{p+t}, with λ = 2, 4, 6 because of the selection rules of the electric dipolar transitions:[227]

$$S_{ED} = \sum_{\lambda=2,4,6} \Omega_\lambda \left| \left\langle 4f^N(\gamma SL)J \left\| U^\lambda \right\| 4f^N(\gamma' S' L')J' \right\rangle \right|^2 \qquad \text{Eq. 7.19}$$

The U^{λ}_{p+t} elements associated to each ion are essentially the same for all matrices, crystals and glasses, because the eigen-states of the free ion are slightly different from the host matrix. These are listed in the literature.[234,236,237]

The Judd-Ofelt parameters characterise the radiative properties of the lanthanide studied in a specific matrix. They include contributions by the crystal field, interconfigurational radial integrals, the mean energy of separation of the configuration of opposite parity, and the dependence on the matrix. The Judd-Ofelt parameters are expressed as follows:

$$\Omega_\lambda = (2\lambda+1) \sum_{k=odd,t} \left| A^t_k \right|^2 \Xi^2(k,t)(2t+1)^{-1} \qquad \text{Eq. 7.20}$$

where:

$$\Xi(t,\lambda) = 2\sum (-1)^{l+l'}(2l+1)(2l'+1) \begin{Bmatrix} 1 & \lambda & t \\ l & l' & l \end{Bmatrix} \begin{pmatrix} l & 1 & l' \\ 0 & 0 & 0 \end{pmatrix} \begin{pmatrix} l' & t & l \\ 0 & 0 & 0 \end{pmatrix} \frac{\langle nl|r|n'l'\rangle \langle nl|r^t|n'l'\rangle}{\Delta E} \qquad \text{Eq. 7.21}$$

With all these considerations we can express the electric dipolar oscillator strength as:

$$f_{ED} = \chi \left[\frac{8\pi^2 mc}{h} \right] \frac{1}{3\bar{\lambda}(2J+1)} \sum_{\lambda=2,4,6} \Omega_\lambda \left| \left\langle 4f^N(\gamma SL)J \left\| U^\lambda_{p+t} \right\| 4f^{N'}(\gamma S' L')J' \right\rangle \right|^2 \qquad \text{Eq. 7.22}$$

From the experimental measurements of the optical absorption spectroscopy at room temperature, we can extract the area under the line that configures the multiplet, the absorption cross-section ($\Gamma_{JJ'}$), for all transitions in the lanthanide ion. This area can be obtained by integrating the

optical absorption coefficient over the spectral region occupied by the multiplet. We can also extract the mean wavelength of each multiplet ($\bar{\lambda}$), calculated from the optical absorption measurements at 6K, with this expression:

$$\left(\bar{\lambda}\right)^{-1} = \frac{\sum_i \Gamma_i / \lambda_i}{\sum_i \Gamma_i} \qquad \text{Eq. 7.23}$$

where Γ_i and λ_i are the area of each peak of the spectrum and the wavelength where it is centred, respectively. The sum is extended to all the peaks of the multiplet.

From these parameters we can calculate the experimental oscillator strength using the following expression:

$$f_{ED,exp} = \frac{2m_e c}{\alpha_f h N \bar{\lambda}^2} \Gamma_{JJ'} \qquad \text{Eq. 7.24}$$

where N is the active ion concentration in the crystalline matrix and α_f is the fine structure constant.

The Judd-Ofelt parameters are obtained by a minimum square fitting of the differences between the experimental oscillator strength and the calculated oscillator strength. The condition given is:

$$\frac{\partial}{\partial \Omega_k} \sum_{J=1}^{q} \left(f_{ED,th} - f_{ED,exp}\right)^2 = 0 \qquad \text{Eq. 7.25}$$

where q is the number of transitions considered in the fitting.

The Judd-Ofelt parameters are then used to calculate, in a theoretical way, additional parameters such as the spontaneous emission probabilities ($A_{JJ'}$) of every transition, from the expression:

$$A_{JJ'} = \chi \left[\frac{32\pi^3 c \alpha_f}{3\bar{\lambda}^3} \right] \frac{n^2}{(2J+1)} \sum_{\lambda=2,4,6} \Omega_\lambda \left| \left\langle 4f^N (\gamma SL) J \left\| U^\lambda \right\| 4f^{N'} (\gamma S' L') J' \right\rangle \right|^2 \qquad \text{Eq. 7.26}$$

From these $A_{JJ'}$, we can calculate other theoretical radiative properties, such as the distribution coefficients of luminescence ($\beta_{JJ'}$) and the radiative lifetime (τ_{rad}), which are interesting for determining the efficiency of lasers and amplifiers using the following expressions:

$$\beta_{JJ'} = \frac{A_{JJ'}}{\sum_{J'} A_{JJ'}} \qquad \text{Eq. 7.27}$$

$$\tau_{rad} = \frac{1}{\sum_{J'} A_{JJ'}} \qquad \text{Eq. 7.28}$$

where the sum are extended to all the transitions to the terminal state J'.[238,239]

7.2.2.2. Judd-Ofelt calculations.

We did the Judd-Ofelt analysis with the experimentally measured oscillator strength from polarised and unpolarised optical absorption spectra of the Er^{3+}-doped RTP:Nb crystals.

In Table 4 of *paper V*, we showed the oscillator strengths and the gravity centres (mean wavelength) for the different multiplets of Er^{3+} in the RTP:(Nb,Er) crystal obtained from the unpolarised optical absorption studies. This paper also included the Judd-Ofelt parameters calculated with these data. These parameters were calculated using the matrix elements $\left\langle \left\| U^{\lambda} \right\| \right\rangle_{JJ'}$ calculated by Kaminskii,[233] and the following refractive indexes:[121]

$$n = \left(n_x^2 + n_y^2 + n_z^2\right)^{1/2} \qquad \text{Eq. 7.29}$$

If the optical absorption of the active ion is dichroic, then if the intensity of the absorption depends on the orientation of the polarisation of the incident light, the Judd-Ofelt theory is not valid. But if we approximate the symmetry of the active centre to an uniaxic symmetry, we can evaluate the absorption of each configuration of polarisation independently, with the electric field of the incident beam parallel (π polarisation) or normal (σ polarisation) to the optical axis of the active centre.

The mean absorption cross-section will be given by:[240]

$$\Gamma = \frac{\Gamma_{\pi} + 2\Gamma_{\sigma}}{3} \qquad \text{Eq. 7.30}$$

where Γ_{π} and Γ_{σ} represent the absorption cross-section corresponding to the various configurations of the polarisation of the incident light. Γ_{σ} contributes twice because two of the three absorption spectra are equal.

We must also redefine Lorentz's correction in the following way:

$$\chi = \frac{\chi_\pi + 2\chi_\sigma}{3} \qquad \text{Eq. 7.31}$$

where $\chi_{\pi,\sigma} = \frac{\left(n_{\pi,\sigma}^2 + 2\right)^2}{9n_{\pi,\sigma}}$ with n_π and n_σ as the ordinary and extraordinary refractive indexes corresponding to the crystallographic directions parallel or normal to the optical axis of the active centre.

Then, with the new Judd-Ofelt parameters ($\Omega_{i,\,(\pi,\sigma)}$) we can calculate the mean effective Judd-Ofelt parameters:

$$\Omega_{i,eff} = \frac{\Omega_{i,\pi} + 2\Omega_{i,\sigma}}{3} \qquad \text{Eq. 7.32}$$

If we extrapolate these considerations to our crystal and take into account the three configurations of polarisation, we obtain the following expression:

$$\Omega_{i,eff} = \frac{\Omega_{i,a} + \Omega_{i,b} + \Omega_{i,c}}{3} \qquad \text{Eq. 7.33}$$

Table 7.2 shows the oscillator strengths and the gravity centres for the different multiplets of Er^{3+} in the RTP:(Nb,Er) crystal obtained from the polarised optical absorption spectra. We compared the energy position of the gravity centre of each multiplet of Er^{3+} in KTP, RTP and RTP:Nb hosts. We found that the difference between the position of these gravity centres was small. There was a maximum deviation of 5.9 nm for the $^4I_{11/2}$ multiplet and the minimum deviation for the gravity centres of the $^2H_{9/2}$ multiplet. Similarly, the splitting of each energy level into its sublevels was similar in all these crystals, which indicates that the crystal field was practically the same, and that there were no significant changes when Nb was introduced into the matrix.

Table 7.2. *Oscillator strengths and average wavelengths for different multiplets of Er^{3+} in the RTP:(Nb,Er) crystal obtained from the polarised optical absorption spectra.*

	Polarisation // *a*		**Polarisation // *b***		**Polarisation // *c***	
$^{2S+1}L_J$	$\int\alpha(\lambda)d\lambda$	$\bar{\lambda}$ **(nm)**	$\int\alpha(\lambda)d\lambda$	$\bar{\lambda}$ **(nm)**	$\int\alpha(\lambda)d\lambda$	$\bar{\lambda}$ **(nm)**
$^4G_{9/2}$	0.44	366.7	2.67	365.3	2.67	365.9
$^4G_{11/2}$	3.67	379.3	25.76	378.7	28.68	378.1
$^2H_{9/2}$	0.14	406.9	0.23	407.3	0.29	407.1
$^4F_{3/2}$	0.05	444.9	0.03	443.5	0.06	443.6
$^4F_{5/2}$	0.09	450.5	0.06	451.9	0.15	452.1
$^4F_{7/2}$	0.67	494.0	0.95	487.9	1.48	491.8
$^2H_{11/2}$	3.78	520.2	17.77	519.8	15.51	519.7
$^4S_{3/2}$	0.53	547.3	1.89	547.6	2.04	547.8
$^4F_{9/2}$	0.77	651.2	1.11	655.1	1.51	656.1
$^4I_{9/2}$	0.01		0.18	799.5	0.02	797.0
$^4I_{11/2}$	0.51	966.2	1.21	976.0	1.20	978.8
$^4I_{13/2}$	9.26	1531.2	6.65	1533.3	10.25	1530.6

Table 7.3 shows the Judd-Ofelt parameters obtained in our crystals and the values obtained in different matrices. We calculated the Judd-Ofelt parameters in our simulation by excluding the $^4I_{13/2}$ multiplet, due to its magnetic dipolar character, and by considering the refractive indexes of the RTP:Nb matrix (see Chapter 6). Except in the case of Ω_6, these were smaller than those obtained in KTP:Er and RTP:Er crystals[121] and those obtained with the unpolarised data. However, the *rms* deviation was higher than that of the unpolarised data, because to obtain these new Judd-Ofelt parameters we included new low-intensity multiplets in the calculation. We also compared the error in calculating these parameters when the $^4I_{13/2}$ multiplet was considered and when it was not. We found that the value of Ω_2 and the error associated to the calculation were lower when the multiplet was not considered. In fact, these Judd-Ofelt parameters were very similar to those obtained in other phosphate matrices.

From these Judd-Ofelt parameters, we obtained other theoretical parameters for the fluorescence properties of Er^{3+} in RTP:(Nb,Er) crystals. However, we had to assume two further approximations: that the material was isotropic and that we only had one active centre. The error introduced when using these approximations was lower than that introduced by considering the low-intensity absorption multiplets.[228] However, in our case there was no overlap between the multiplets of the optical absorption spectra as there was in other matrices.[243] In this way we eliminate a possible source of error, because when there is overlap we cannot distinguish between the contributions of the different multiplets.

Table 7.3. *Judd-Ofelt parameters of Er^{3+} in the RTP:(Nb,Er) crystal and in other phosphate matrices.*

Matrix		$\Omega_2 \cdot 10^{-20}$ (cm^2)	$\Omega_4 \cdot 10^{-20}$ (cm^2)	$\Omega_6 \cdot 10^{-20}$ (cm^2)	Reference
RTP:Nb		5.15	0.56	0.23	
RTP		20.5	1.60	1.83	[121]
KTP		38.9	2.93	1.33	[121]
Phosphates		9.31	3.51	1.28	[121]
		5.42	1.55	0.98	[241]
Fluorophosphate glasses	High F^- concentration	2.75	1.69	1.15	[241]
	Low F^- concentration	3.39	1.79	1.2	[241]
Metaphosphate glasses	FP4	2.94	1.37	1.50	[242]
	FP8	3.25	1.41	1.49	[242]
	FP20	4.71	1.61	1.62	[242]
	FP20/Pb	3.82	1.52	1.33	[242]
	KBaP	6.22	1.52	1.02	[242]
	CaZnBaP	5.85	1.41	0.84	[242]

Table 7.4 shows the probability of electric dipolar transition (A_{ED}), the distribution coefficients of luminescence (β_{ij}) and the radiative lifetime (τ) calculated with our Judd-Ofelt parameters.

Table 7.4. *Radiative properties of erbium in RTP:(Nb,Er) crystals.*

	λ (nm)	Energy (cm^{-1})	A_{ED} (s^{-1})	β_{ij} (%)	τ_{rad} (μs)
$^4G_{9/2} \rightarrow {}^4G_{11/2}$	9250	1081	0	0	20
$^2H_{9/2}$	3464	2887	2	0	
$^4F_{3/2}$	2043	4895	9	0	
$^4F_{5/2}$	1849	5409	93	0.2	
$^4F_{7/2}$	1397	7158	784	1.6	
$^2H_{11/2}$	1213	8240	119	0.2	
$^4S_{3/2}$	1122	8913	39	0.1	
$^4F_{9/2}$	833	12001	1690	3.5	
$^4I_{9/2}$	668	14975	70	0.1	
$^4I_{11/2}$	584	17131	1987	4.1	
$^4I_{13/2}$	479	20893	41160	84.4	
$^4I_{15/2}$	365	27397	2811	5.8	
$^4G_{11/2} \rightarrow {}^2H_{9/2}$	5537	1806	5	0	14
$^4F_{3/2}$	2621	3814	1	0	
$^4F_{5/2}$	2310	4328	2	0	
$^4F_{7/2}$	1645	6077	65	0.1	
$^2H_{11/2}$	1397	7159	18	0	
$^4S_{3/2}$	1277	7832	17	0	
$^4F_{9/2}$	916	10920	1664	2.3	
$^4I_{9/2}$	720	13894	608	0.8	
$^4I_{11/2}$	623	16050	72	0.1	
$^4I_{13/2}$	505	19812	3611	5.0	
$^4I_{15/2}$	380	26316	66679	91.7	
$^2H_{9/2} \rightarrow {}^4F_{3/2}$	4980	2008	0	0	234
$^4F_{5/2}$	3965	2522	1	0	

	$^4F_{7/2}$	2341	4271	30	0.7	
	$^2H_{11/2}$	1868	5353	27	0.7	
	$^4S_{3/2}$	1659	6026	0	0	
	$^4F_{9/2}$	1097	9114	28	0.7	
	$^4I_{9/2}$	827	12088	99	2.3	
	$^4I_{11/2}$	702	14244	608	14.2	
	$^4I_{13/2}$	555	18006	2481	58.1	
	$^4I_{15/2}$	407	24510	994	23.3	
$^4F_{3/2} \rightarrow$	$^4F_{5/2}$	19455	514	0	0	700
	$^4F_{7/2}$	4419	2263	1	0	
	$^2H_{11/2}$	2989	3345	0	0	
	$^4S_{3/2}$	2489	4018	14	1	
	$^4F_{9/2}$	1407	7106	12	0.9	
	$^4I_{9/2}$	992	10080	220	15.4	
	$^4I_{11/2}$	817	12236	173	12.1	
	$^4I_{13/2}$	625	15998	82	5.7	
	$^4I_{15/2}$	444	22502	926	64.8	
$^4F_{5/2} \rightarrow$	$^4F_{7/2}$	5717	1749	3	0.1	467
	$^2H_{11/2}$	3532	2831	2	0.1	
	$^4S_{3/2}$	2854	3504	2	0.1	
	$^4F_{9/2}$	1517	6592	73	3.4	
	$^4I_{9/2}$	1045	9566	114	5.3	
	$^4I_{11/2}$	853	11722	87	4.0	
	$^4I_{13/2}$	646	15484	859	40.1	
	$^4I_{15/2}$	455	21988	1001	46.7	
$^4F_{7/2} \rightarrow$	$^2H_{11/2}$	9242	1082	1	0	360
	$^4S_{3/2}$	5698	1755	0	0	
	$^4F_{9/2}$	2065	4843	8	0.3	
	$^4I_{9/2}$	1279	7817	107	3.8	
	$^4I_{11/2}$	1003	9973	161	5.8	
	$^4I_{13/2}$	728	13735	360	13.0	
	$^4I_{15/2}$	494	20239	2138	77.0	
$^2H_{11/2} \rightarrow$	$^4S_{3/2}$	14859	673	0	0	56
	$^4F_{9/2}$	2659	3761	55	0.3	
	$^4I_{9/2}$	1485	6735	204	1.1	
	$^4I_{11/2}$	1125	8891	104	0.6	
	$^4I_{13/2}$	790	12653	194	1.1	
	$^4I_{15/2}$	522	19157	17290	96.9	
$^4S_{3/2} \rightarrow$	$^4F_{9/2}$	3238	3088	0	0	811
	$^4I_{9/2}$	1650	6062	44	3.5	
	$^4I_{11/2}$	1217	8218	24	1.9	
	$^4I_{13/2}$	835	11980	331	26.8	
	$^4I_{15/2}$	541	18484	834	67.6	
$^4F_{9/2} \rightarrow$	$^4I_{9/2}$	3362	2974	12	1.0	839
	$^4I_{11/2}$	1949	5130	67	5.6	
	$^4I_{13/2}$	1124	8892	70	5.9	
	$^4I_{15/2}$	649	15396	1043	87.5	
$^4I_{9/2} \rightarrow$	$^4I_{11/2}$	4638	2156	1	0.4	6867
	$^4I_{13/2}$	1690	5918	33	22.4	
	$^4I_{15/2}$	805	12422	112	77.2	
$^4I_{11/2} \rightarrow$	$^4I_{13/2}$	2658	3762	17	9.4	5369
	$^4I_{15/2}$	974	10266	169	90.6	
$^4I_{13/2} \rightarrow$	$^4I_{15/2}$	1537	6504	81	100	12392

7.2.3. Emission of Er^{3+}.

Room temperature photoluminescence of Er was achieved after excitation at 499, 521 and 981 nm (20040, 19194 and 10194 cm^{-1}) in an $RbTi_{0.967}Nb_{0.026}Er_{0.007}OPO_4$ sample. Figure 7.3 shows the results obtained.

As we pointed out in *paper IX* the emission around 1550 nm (6452 cm^{-1}) (attributed to the $^4I_{13/2} \rightarrow {}^4I_{15/2}$ transition) was the most intense emission band for Er^{3+} in this crystal. We then focused our attention on this emission band. This transition has applications in remote communication systems and as an amplifier in silicon waveguides.[152] It also has interesting applications as safety-eye radiation because it is absorbed by the eye's aqueous humour, and enhances the security of industrial devices.[244]

It is clear from the low temperature absorption spectra recorded in Section 7.2.1 that at least two kinds of Er^{3+} centres coexist. Therefore, before doing any further analysis of the fluorescence dynamics in RTP:(Nb,Er) crystals, we must check whether the different Er^{3+} centres must be considered separately or whether they can be taken together without any distinction. To do this, we registered the low-temperature (77 K) emission spectrum of the integrated infrared fluorescence around 1550 nm with an excitation between 965-990 nm. Figure 7.4 clearly shows that the spectra are made of more than eight lines. Again, therefore, both types of Er^{3+} centres contribute. As we can see in the close-up of this figure, practically all the peaks comprise a marked peak and a shoulder near its basis.

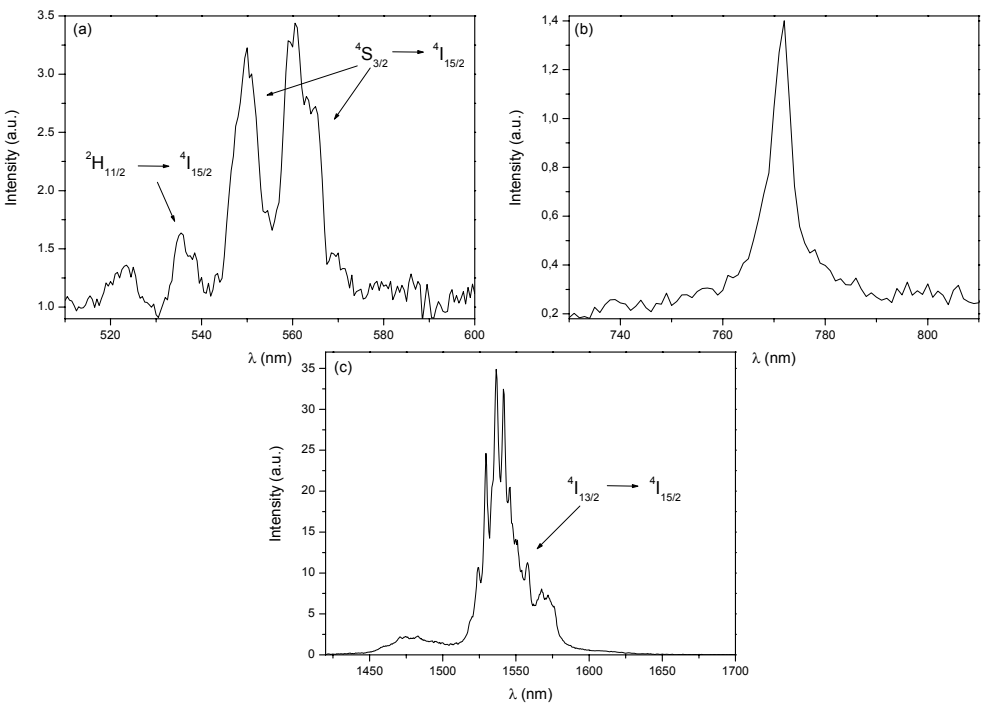

Figure 7.3. *Different emissions of Er^{3+} in RTP:(Nb,Er) crystals recorded at room temperature after excitations at (a) 499 nm, (b) 521 nm and (c) 981 nm.*

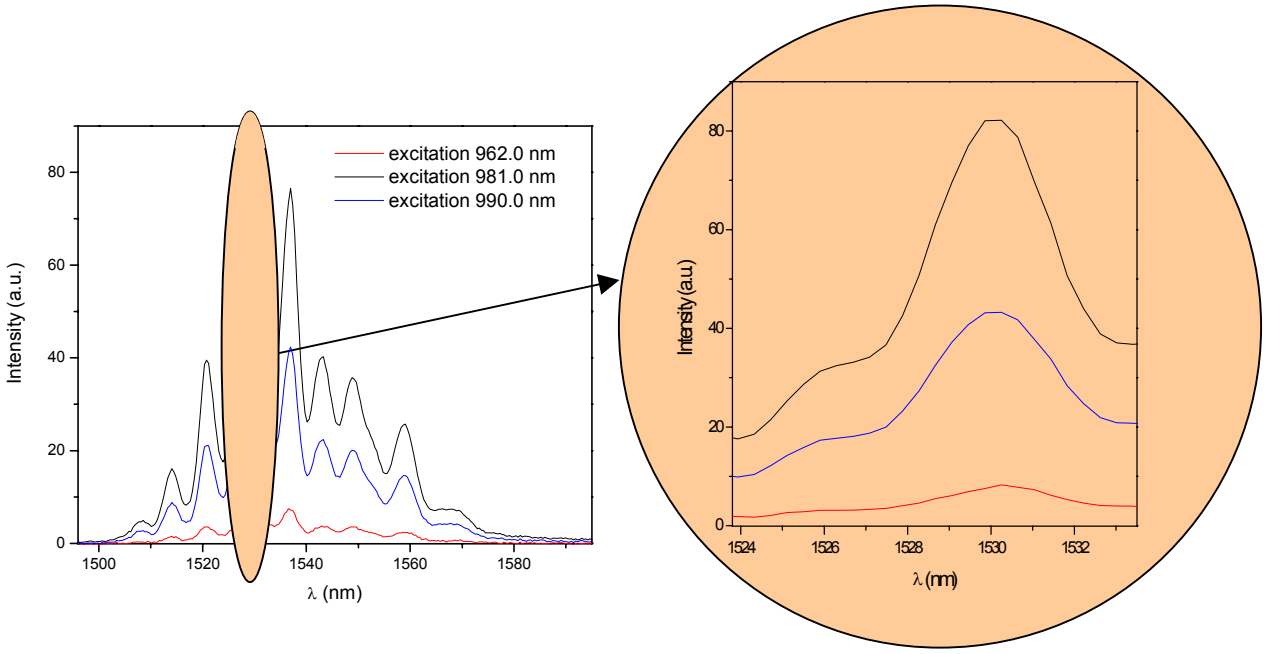

Figure 7.4. *Variation of the emission spectrum of the transition* $^4I_{11/2} \rightarrow {}^4I_{15/2}$ *with the excitation wavelength collected at 77 K. Magnification of the area between 1523 and 1535 nm corresponding to the structure of the most intense peak of the spectrum.*

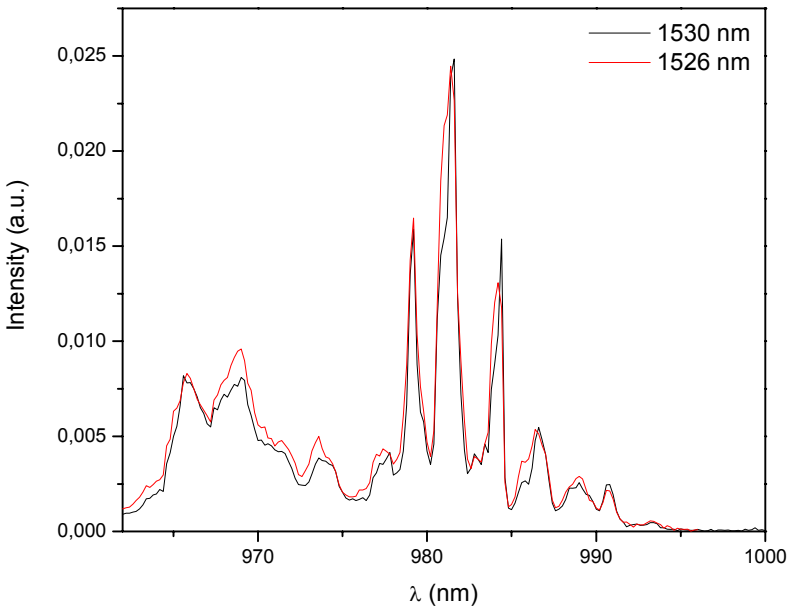

Figure 7.5. *Excitation spectra of* Er^{3+} *in RTP:(Nb,Er) crystals corresponding to the* $^4I_{9/2}$ *multiplet measured at 1526 and 1530.3 nm at 77 K.*

We then registered the excitation spectra at 1526.0 and 1530.8 nm, corresponding to the wavelengths of the shoulder and the maximum of the peak. Figure 7.5 shows the results of these

measurements. There was clearly an increase in the absorption lines around 981.0, 984.0 and 985.6 nm when the excitation spectrum was collected at 1526 nm.

We then have chose the most intense peak of these spectra and collected the fluorescence for the transition $^4I_{13/2} \rightarrow {}^4I_{15/2}$ by modifying the excitation wavelength in two-angstrom steps between 980.2 and 982.4 nm. We found that there was a slight difference in relative intensity between the two most intense peaks of these fluorescence spectra (see Figure 7.6). This figure shows that at an excitation wavelength of 981.6 nm, the intensities of the two most intense peaks in these luminescence spectra, which up to this excitation wavelength had been different, became equal. All these findings show that at least two centres of Er^{3+} are present in this crystal. However, the changes in the spectroscopic properties introduced by the different centres are so small that their effects on the fluorescence spectra overlap, so in what follows we will make no distinction between the two Er^{3+} centres.

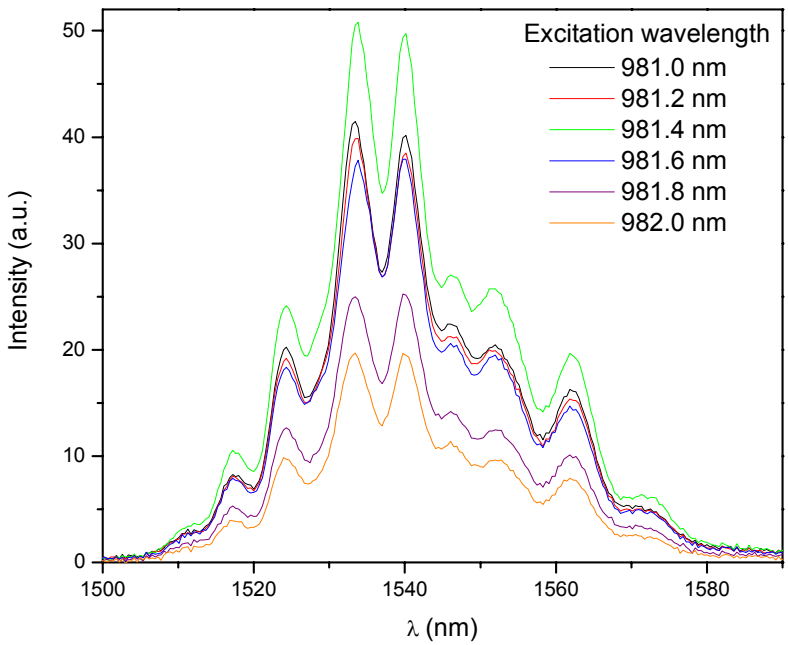

Figure 7.6. *Variation of the $^4I_{13/2} \rightarrow {}^4I_{15/2}$ emission of Er^{3+} in RTP:(Nb,Er) crystals with the excitation wavelength in the range 980.2-982.4 nm at 77 K*

Figure 7.7 compares the experimental infrared emission ($^4I_{13/2} \rightarrow {}^4I_{15/2}$ transition) in the three polarisation configurations obtained at room temperature after an excitation in the green, where Er^{3+} shows a high absorption cross-section. The shapes and intensities of all three spectra are very similar, so these crystals might be used in applications where the polarisation of the outgoing emission is important.

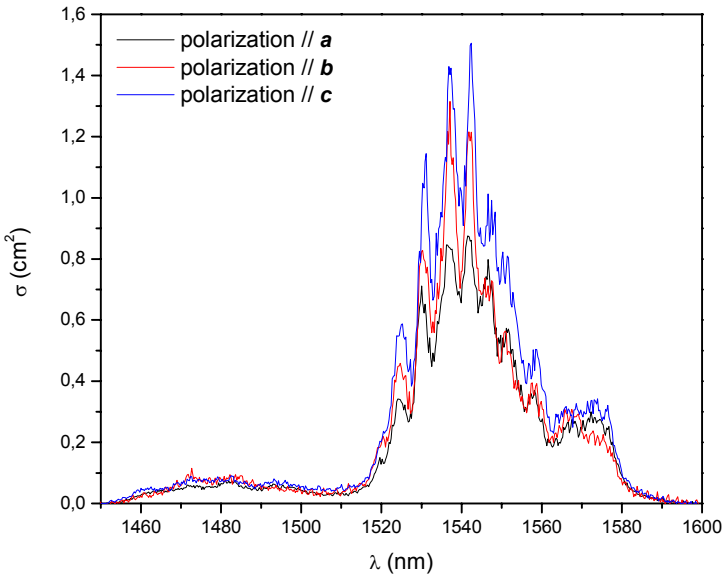

Figure 7.7. *$^4I_{13/2} \rightarrow {}^4I_{15/2}$ polarised emission cross section of Er^{3+} in RTP:(Nb,Er) crystals recorded at room temperature after excitation in the green.*

We studied the photoluminescence of erbium at low temperature to determine the splitting of the ground energy level of erbium. Figure 7.8 shows the 70 K emission corresponding to the $^4I_{13/2} \rightarrow {}^4I_{15/2}$ transition.

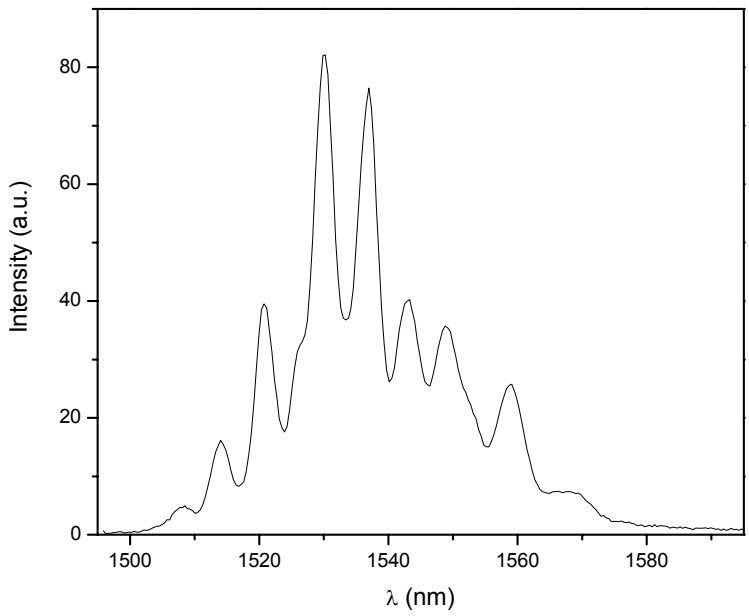

Figure 7.8. *$^4I_{13/2} \rightarrow {}^4I_{15/2}$ emission of Er^{3+} in RTP:(Nb,Er) crystals at 70 K after excitation at 981 nm.*

The number of sublevels expected by the maximum number of Kramers levels due to the effect of the crystal field is eight. These clearly appear in the spectrum with energy values of 1524.2, 1529.6, 1536.6, 1541.8, 1545.9, 1550.5, 1557.9 and 1567.5 nm (6561, 6538, 6508, 6486, 6469, 6449, 6419 and 6379 cm^{-1}). The spectrum also shows minor peaks and shoulders that may be related to the presence of more than one Er^{3+} centre in this crystal, as well as to the transition from the second sublevel of the $^4I_{13/2}$ to the sublevels of the ground level. From these energy positions we obtained the splitting of the ground energy sublevel of erbium. We used these results to schematise the emission channels around 1.5 μm and the energy position of all the sublevels of the ground level in Figure 7.9. Figure 7.10 shows the general crystal field splitting of Er^{3+} in $RbTi_{0.967}Nb_{0.026}Er_{0.007}OPO_4$ as an interpretation of the absorption and emission lines observed. As there is more than one centre of Er^{3+} in these crystals, it is difficult to assign them in an only way. The same figure shows the emissions observed in this crystal. All emissions could be assigned except the one that corresponded to Figure 7.3 (b) around 770 nm (12987 cm^{-1}). This emission fitted very well with the second harmonic generation of the emission at around 1540 nm, which led to think of this possibility. However, we did not specifically study this emission to confirm this supposition.

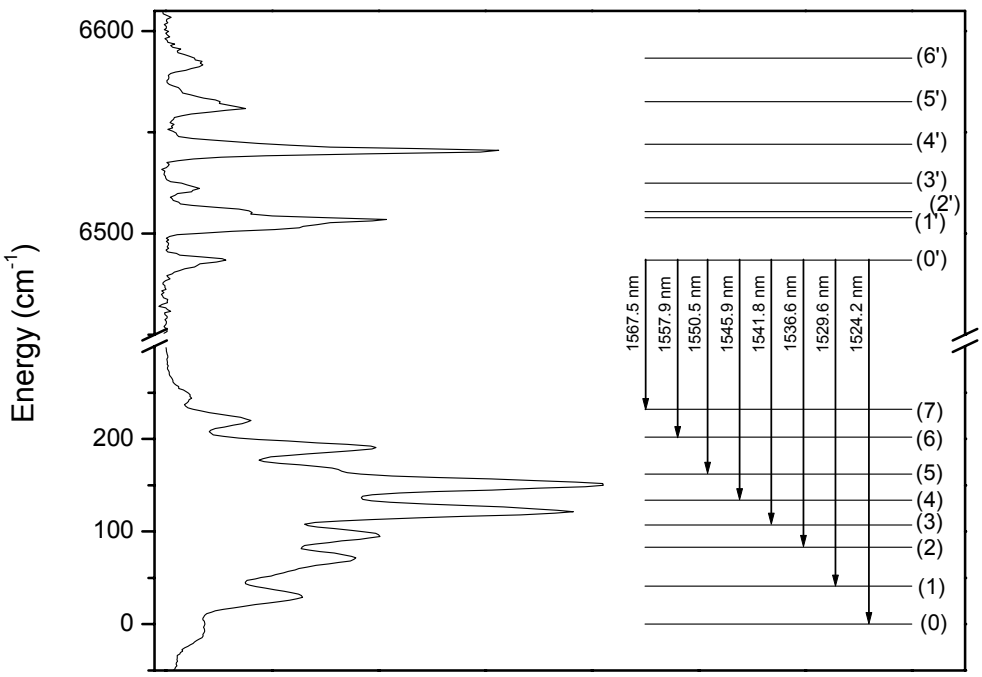

Figure 7.9. *Schematised emission channels of erbium around 1.5 μm.*

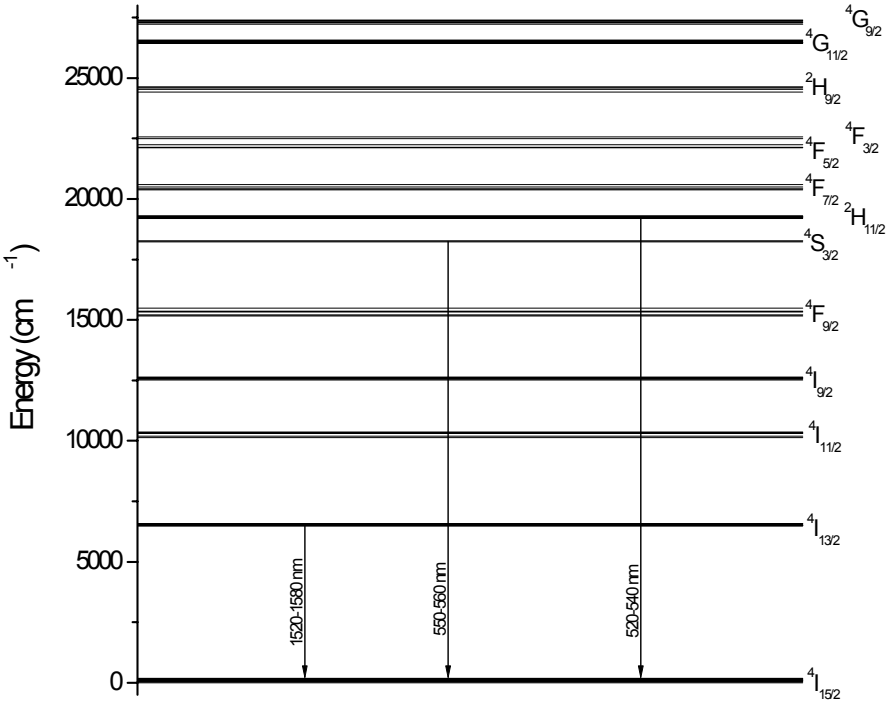

Figure 7.10. *Schematised diagram of energetic levels of Er^{3+} in RTP:(Nb,Er) crystals.*

We measured the lifetime of the emissions corresponding to the $^2H_{11/2} \rightarrow {}^4I_{15/2}$, $^4S_{3/2} \rightarrow {}^4I_{15/2}$ and $^4I_{13/2} \rightarrow {}^4I_{15/2}$, transition at 535 and 560 nm after excitation at 521 nm. We also checked the lifetime of the two centres of Er^{3+} by measuring the lifetime at 1530 and 1526 nm after excitation at 981.6 nm. The lifetimes measured for the same transitions under different excitation wavelengths were practically the same (see Table 7.5), although there was a slight difference in the lifetimes measured at 1530 and 1526 nm, which corresponded to the two different centres of Er^{3+} in the crystal. All the decay curves were single exponential, so non-radiative processes were not very important for the $^4I_{13/2}$ emission.

Table 7.5. *Lifetimes of the emissions observed for Er^{3+} in RTP:(Nb,Er) crystals.*

Excitation wavelength (nm)	Transition	Collecting wavelength (nm)	τ_r (ms)
490	$^2H_{11/2} \rightarrow {}^4I_{15/2}$	535	0.7
521	$^4S_{3/2} \rightarrow {}^4I_{15/2}$	560	1.0
981.6	$^4I_{13/2} \rightarrow {}^4I_{15/2}$	1530	6.7
981.6	$^4I_{13/2} \rightarrow {}^4I_{15/2}$	1526	7.2

7.3. Optical properties of Yb^{3+} in $RbTiOPO_4$:Nb crystals.

Ytterbium has many advantages as a dopant in a non-linear optical crystal host such as RTP. The 1 μm fundamental laser output can be transferred to the frequency-doubled green wavelength directly, without the need for another non-linear crystal and without losses in the green because Yb^{3+} has no absorption at the doubled wavelength.[224] Because there are few Yb^{3+} states, we cannot use the Judd-Ofelt theory to predict the radiative transition probability. Therefore, we did not make a theoretical simulation of the spectroscopic properties of this ion.

7.3.1. Optical absorption of Yb^{3+}.

We studied the polarised optical absorption of Yb^{3+} in RTP:Nb crystals at room temperature and 6 K. Yb^{3+} has a clear absorption band between 800 and 1000 nm (12000 and 10000 cm^{-1}) that is associated with the transition $^2F_{7/2} \rightarrow {}^2F_{5/2}$. In Figure 5 in *paper II*, Figure 4 in *paper IV* and Figure 7 in *paper VI* we show the room temperature absorption coefficient of this transition, measured for all three polarisations in an $RbTi_{0.935}Nb_{0.043}Yb_{0.022}OPO_4$ crystal. The room temperature absorption is characterised by three main peaks centred at 902, 955 and 972 nm (11086, 10471 and 10288 cm^{-1}, respectively) for all three configurations. In the case of E // ***a***, the peak centred at 902 nm shifted slightly towards 903 nm (11074 cm^{-1}), which perhaps indicates a low disorganisation of the crystal. However, the other two peaks were well centred in all three configurations. Note that the absorption coefficient depended strongly on the light polarisation and was maximal for E // ***c*** and minimal for E // ***a*** at 902 nm, and maximal for E // ***b*** and minimal for E // ***a*** at 972 nm. Clearly, then, there was a strong dichroism in these crystals, as we have explained in these papers. We should mention that the intensity of the Yb^{3+} absorption in this crystal was about one order of magnitude larger than had previously been achieved in $KTiOAsO_4$ crystals,[207] because the concentration of Yb^{3+} in our crystal was 14 times higher. The maximum absorption cross-sections at 972 nm (zero line), calculated with the Yb^{3+} concentration of 1.66×10^{20} ions·cm^{-3}, were 3.25×10^{-21} cm^2 for E // ***c*** (linewidth 3.8 nm), 7.09×10^{-21} cm^2 for E // ***b*** (linewidth 4.5 nm), and 2.08×10^{-21} cm^2 for E // ***a*** (linewidth 3.8 nm). The large splitting shown by the absorption spectrum (around 70 nm) was similar only to that obtained in Yb-doped fluoroapathites,[245] which indicates, as we explained in *paper X*, that a broadband fluorescence can be obtained that is interesting for tunability and subpicosecond-pulse generation applications.

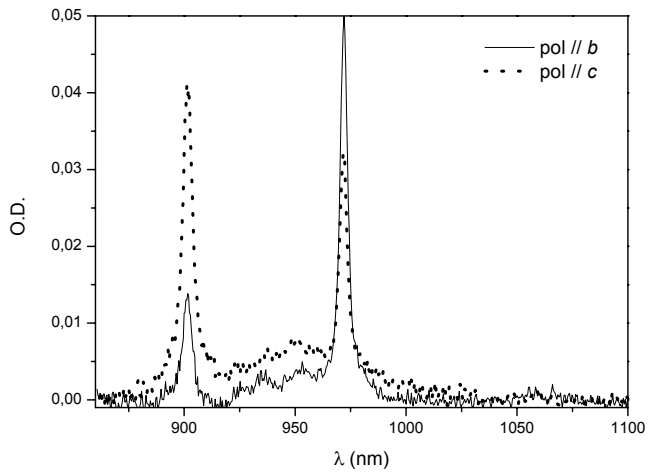

Figure 7.11. *Optical absorption of Yb^{3+} in RTP:(Nb,Yb) at 6K.*

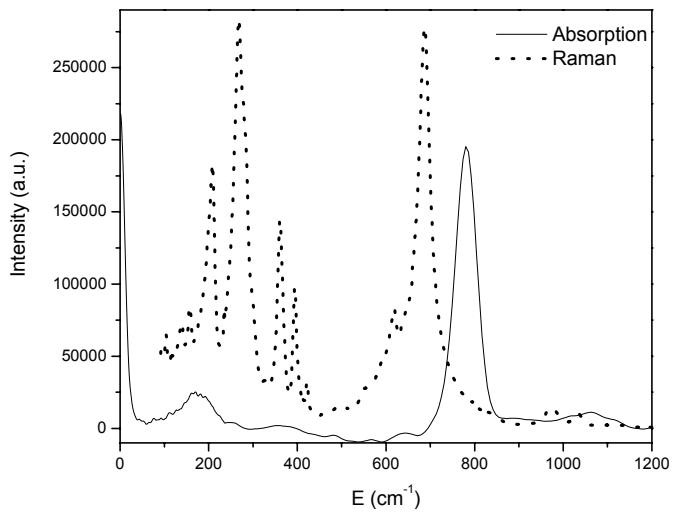

Figure 7.12. *Comparison of the optical absorption of Yb^{3+} in RTP:(Nb,Yb) at 6K and the Raman scattering of the crystal.*

To accurately determine the energy sublevels of ytterbium in this crystal, we measured the optical absorption spectrum down to 6 K. As ytterbium also has an odd number of electrons in the 4*f* shell, polarisation-dependent selection rules for the electronic transitions are not expected (as with Er^{3+}). Also, the number and positions of the absorption peaks have to be independent of the polarisation, but the intensity of the peaks associated with the three polarisations can still vary. Then, as future applications of these crystals will not be developed at 6 K, we do not need to take the polarised spectra in the three principal axes of this ion at this temperature. Figure 7.11 shows the low-temperature absorption at 6 K of Yb^{3+} in $RbTi_{0.935}Nb_{0.043}Yb_{0.022}OPO_4$. At low temperature, the most populated Stark level is the lowest sublevel of the ground state $^2F_{7/2}$ (0), so the bands observed at 6 K can be associated with transitions from this sublevel to the three Stark levels of the excited state $^2F_{5/2}$

(denoted as $^2F_{5/2}$ (0'), (1'), and (2') in order of increasing energy) located at 903.4 nm (11069 cm^{-1}), 955.0 nm (10471 cm^{-1}) and 971.9 nm (10289 cm^{-1}), with a respective linewidth of 5.5, 7.2 and 2.4 nm. We also checked for the phonon-electron-coupled transitions, which are important in the Ln^{3+} ions at the beginning and end of the lanthanide series.[246] Since the maximum cross-section of the zero line transition at 972 nm in Figure 7.11 increases when the temperature decreases, and since there is no band shifting at 6K, resonant interactions are not implied between the (0) → (0') transition and some Raman modes. This is clear when we compare the absorption spectrum of Yb^{3+} in RTP:Nb crystals and the Raman scattering of this crystal (see Figure 7.12).

7.3.2. Emission of Yb^{3+}.

Room- and low- temperature fluorescence spectra of Yb^{3+} in $RbTi_{0.935}Nb_{0.043}Yb_{0.022}OPO_4$ were measured in 90º geometry with excitation at 972 nm. Figure 7.13 shows the room temperature emission spectra for all three polarisations, exciting was done at the centre of the sample and the *E* // ***b*** spectrum was doubly recorded in order to better compare the spectra. The peaks in the measured spectra correspond to the emission from the excited $^2F_{5/2}$ manifold to the four sublevels of the ground state manifold $^2F_{7/2}$. The maximum at 972 nm (10288 cm^{-1}), which appears in all the spectra, is due to the $^2F_{5/2}(0') \rightarrow {}^2F_{7/2}(0)$ transition. The position of this peak determines the energy of the $^2F_{5/2}(0')$ sublevel. These spectra are characterised by a broadband fluorescence, as we explained in *paper X*, with peaks at 972 nm (10288 cm^{-1}), 1025 nm (9756 cm^{-1}), 1051 nm (9515 cm^{-1}) and 1071 nm (9337 cm^{-1}). Again we observed the dichroic behaviour typical of these samples, that we explained in *paper X*. We also recorded the emission spectrum of Yb^{3+} in this matrix after excitation at 902 nm, obtaining a similar shape to the one for excitation at 972 nm.

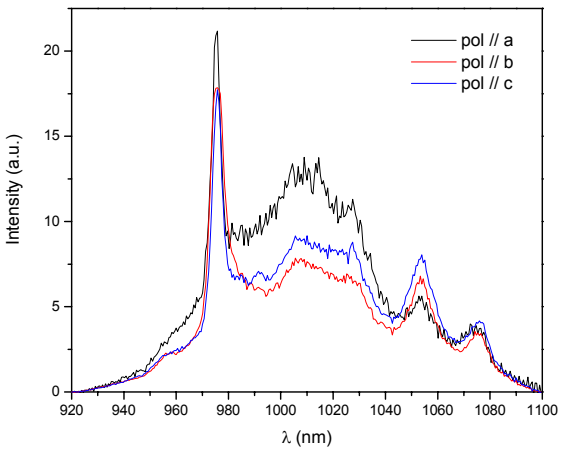

Figure 7.13. *$^2F_{5/2} \rightarrow {}^2F_{7/2}$ polarised emission of Yb^{3+} in RTP:(Nb,Yb) crystals at room temperature after excitation at 972 nm.*

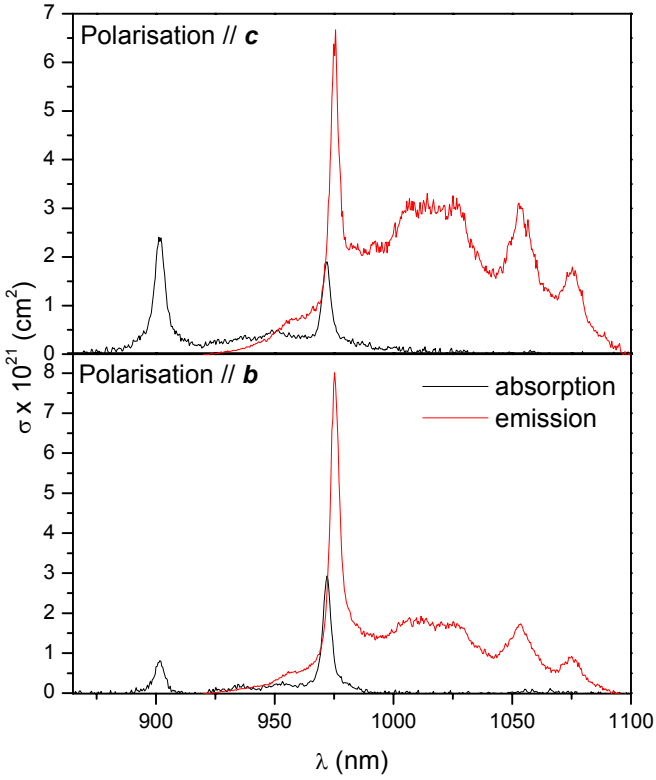

Figure 7.14. *Emission cross-section and absorption cross-section of Yb^{3+} in RTP:(Nb,Yb) crystals at room temperature corresponding to the* ***b*** *and* ***c*** *polarisation configurations.*

We used the Früchtbauer-Ladenburg method to calculate the emission cross-section (σ_e) of this transition using the expression:

$$\sigma_e(\lambda) = \frac{\lambda^4 I(\lambda)}{8\pi n^2 c \tau_f \int I(\lambda) d\lambda} \qquad \text{Eq. 7.34}$$

where $I(\lambda) / \int I(\lambda) d\lambda$ is the normalized line shape function, n is the refractive index, c is the vacuum speed of the light, and τ_f is the spontaneous fluorescence time. This method is a generalisation of the Einstein's phenomenological theory for split states, as it is by effect of the crystal field.

Figure 7.14 compares the absorption and emission cross-sections of Yb^{3+} in $RbTi_{0.935}Nb_{0.043}Yb_{0.022}OPO_4$ at room temperature. It shows that strong reabsorption should be expected at the maximum emission peak at 972 nm (zero line). To obtain the crystal field splitting of the ground state manifold $^2F_{7/2}$, we performed low-temperature polarised emission experiments. Figure 7.15 shows the emission spectra of Yb^{3+} at 9 K. The Stark sublevels of the ground state manifold $^2F_{7/2}$ derived from the 6 K emission spectrum are at 971.9, 1002.0, 1023.7, and 1071.4 nm (10289, 9980, 9768 and 9333 cm^{-1}, respectively).

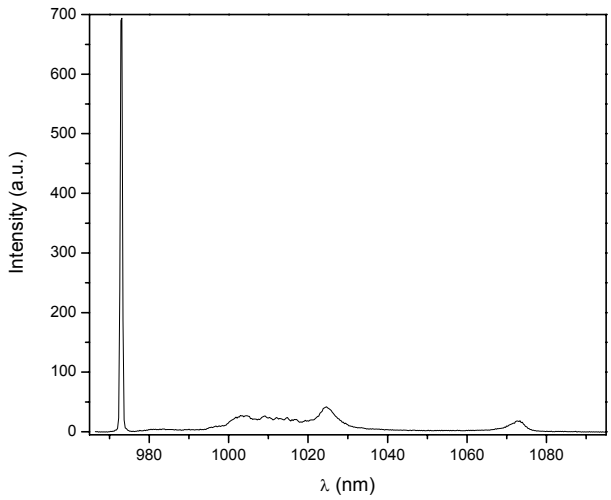

Figure 7.15. *$^2F_{5/2} \rightarrow {}^2F_{7/2}$ unpolarised emission of Yb^{3+} in RTP:(Nb,Yb) crystals at 9 K after excitation at 972 nm.*

However, other lines were also observed. By comparing the luminescence spectrum at low temperature and the Raman scattering of this crystal (see Figure 7.16), we can attribute these lines to electron-phonon coupling between the active ion and the matrix. Electron-phonon interaction has been already reported in several Yb^{3+}-doped systems.[247] In these cases, when the difference between two Stark levels matches the energy of a lattice phonon, a strong vibronic structure can appear in the spectra. This leads to a splitting of the bands and in some cases even makes it difficult to determine the energy level. As this electron-phonon coupling only affects the least intense peaks, we can ignore reabsorption effects related to new transitions from thermally populated ground state sublevels.

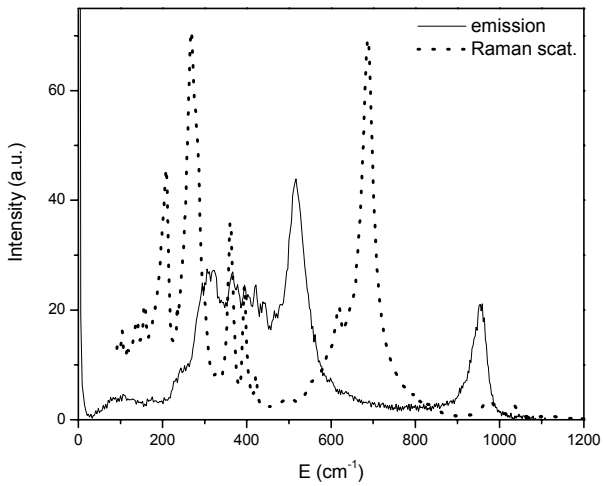

Figure 7.16. *Comparison of the emission of Yb^{3+} in RTP:(Nb,Yb) at 9K and the Raman scattering of the crystal.*

Figure 7.17 shows the crystal field splitting of both manifolds of Yb^{3+} in RTP:Nb crystals, obtained from the low-temperature absorption and emission spectra. The emission lines at room

temperature at about 955 and 1051 nm can be associated with the $^2F_{5/2}$ (1') → $^2F_{7/2}$ (0) and $^2F_{5/2}$ (1') → $^2F_{7/2}$ (3) transitions. The other two transitions from the first Stark sublevel ($^2F_{5/2}$ (1') → $^2F_{7/2}$ (1) and $^2F_{5/2}$ (1') → $^2F_{7/2}$ (2)), expected at 984 and 1005 nm, overlap with the emission lines for the $^2F_{5/2}$ (0') → $^2F_{7/2}$ (1) and $^2F_{5/2}$ (0') → $^2F_{7/2}$ (3) transitions, thus broadening the fluorescence band of Yb^{3+} in RTP:(Nb,Yb) crystals.

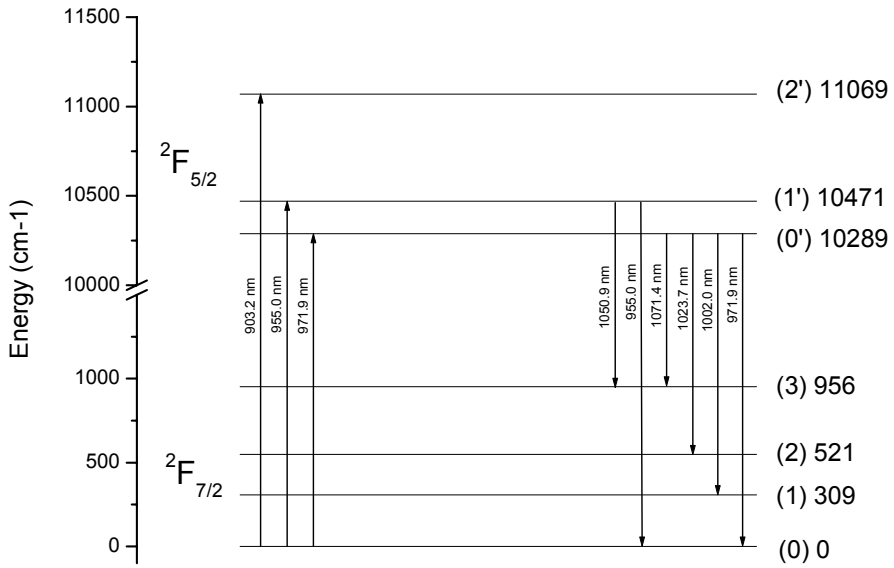

Figure 7.17. *Schematised diagram of energetic levels of Yb^{3+} in RTP:(Nb,Yb) crystals.*

It is important to accurately measure the excited-state lifetime as a further step in the characterisation of RTP:(Nb,Yb) as a laser material. We determined the fluorescence lifetime by collecting the decay of the luminescence intensity of the strongest peak of the luminescence spectra after excitation at 972 nm at room temperature. The fluorescence lifetime curves for these crystals have a single exponential decay behaviour and are quite long (2.2 ms; see Figure 7.18).

Radiation trapping and total internal reflection can strongly affect the measured lifetimes. This is especially a problem in crystals in which there is a lot of overlap between absorption and emission. The term "radiation trapping" usually refers to the effect of reabsorption of the initial emission by ions in the ground state. This reabsorption is followed by reemission and lengthens the measured lifetime. Total internal reflection, which is typical for solids because of their higher refractive indexes, further increases the probability of reabsorption of the emitted photons by ions in the ground state. To eliminate these effects, optically thin samples should be used for lifetime measurements. Even in optically thin samples, however, total internal reflection increases the emission path-length in the crystal and causes the observed lifetimes to artificially lengthen. However, because in our crystals the concentration of Yb^{3+} in the crystals is not very high, these effects can be ignored. The lifetime

measured in a sample containing only a concentration of Yb^{3+} of 6.0×10^{19} ions·cm^{-3} (2.3 ms) confirmed that there was no lengthening of the observed lifetime. Such a long lifetime is interesting for a more efficient inversion of the electronic population of Yb^{3+}, which, as we explained in *paper X*, is needed for efficient power laser emission.

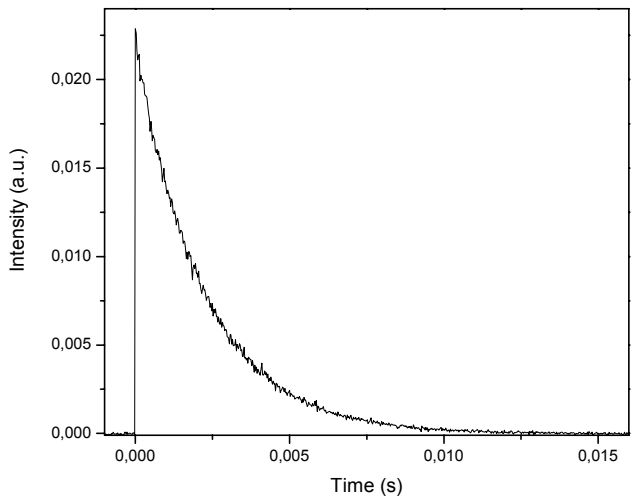

Figure 7.18. *Decay curves of the $^2F_{5/2} \rightarrow {}^2F_{7/2}$ transition in RTP:(Nb,Yb).*

7.3.3. Theoretical lasing parameters of Yb^{3+} in $RbTi_{0.935}Nb_{0.043}Yb_{0.022}OPO_4$.

We can use all these results for the optical absorption and emission of Yb^{3+} in these crystals, to calculate some theoretical parameters that can help us to determine the viability of this crystal for laser applications.

The first parameter that we will study is laser gain (ζ), which is defined as:

$$\zeta = \beta\sigma_e - (1-\beta)\sigma_{abs} \qquad \text{Eq. 7.35}$$

where $\beta = N_1/C$, with N_1 as the electron population of the $^4F_{7/2}$ multiplet and $C = N_0 + N_1$, where N_0 is the electron population of the $^4F_{5/2}$ multiplet. β can only be between 0 and 1. With ζ, we can estimate a priori at which wavelength a laser based on this material will emit. Figure 7.19 shows the results of this analysis. However, no important information can be extracted, because of the broadband fluorescence of this crystal.

Another important spectral parameter for assessing the performance of RTP:(Nb,Yb) lasers is the minimum absorbed pump intensity I_{min}, which is calculated from the following expression:[248]

$$I_{min} = \frac{\sigma_a}{\sigma_e + \sigma_a} \frac{h\nu}{\sigma_{ap}\tau} \qquad \text{Eq. 7.36}$$

where σ_a is the absorption cross-section at the laser wavelength, σ_{ap} is the absorption cross-section at the pump wavelength, σ_e is the emission cross-section at the laser wavelength and τ is the $^2F_{5/2}$ lifetime. This parameter (I_{min}) is used as a figure of merit to indicate the relative usefulness of various ytterbium-doped media.[248]

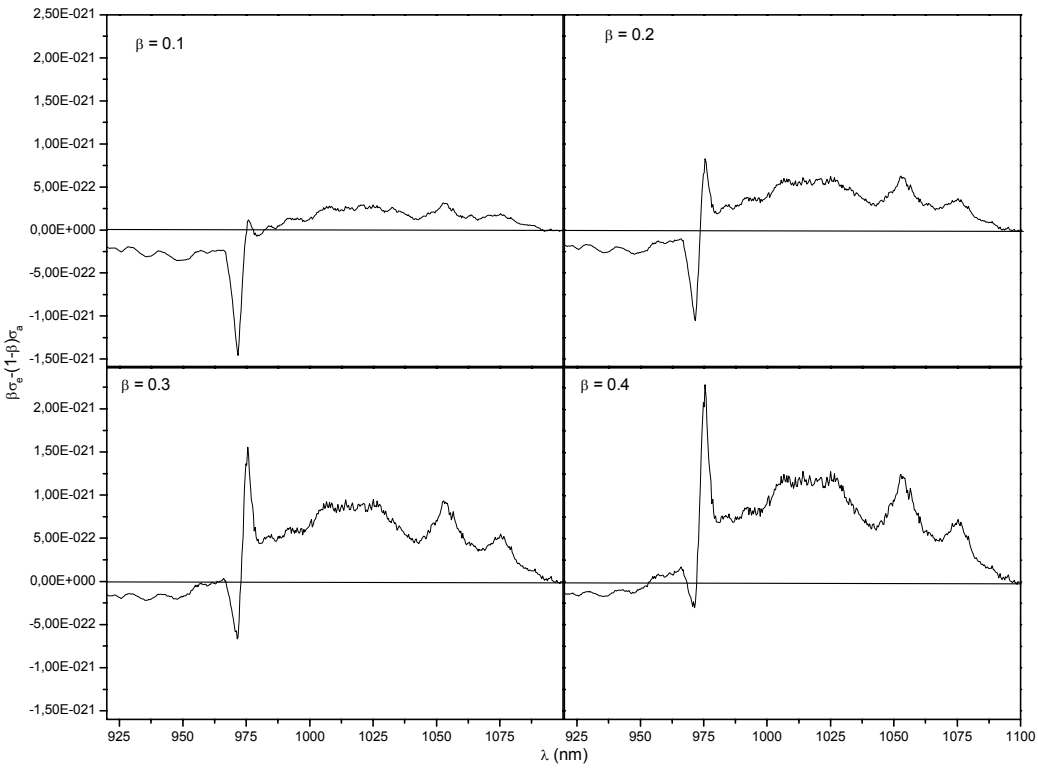

Figure 7.19. *Laser gain of Yb^{3+} in RTP:(Nb,Yb) crystals for β = 0.1-0.4.*

Figure 7.20 shoes, for comparative purposes, the position of RTP:(Nb,Yb) in relation to other Yb-doped materials. We chose 1072 nm as the extraction wavelength to calculate this parameter in RTP:(Nb,Yb). The emission cross-section is proportional to λ^4 by the Früchtbauer-Ladenburg method,[249] and the extraction wavelength needs to be as long as possible to decrease the populations in the lower laser terminal level in quasi-three-level systems.[248] Normally, only for ΔE values above 400 cm^{-1} is it possible for the system to gain enough to achieve population inversion. We should therefore choose the extraction laser output at the longest feasible wavelength if its emission cross-section is suitable. For several ytterbium lasers, the free-running laser output wavelength with low output coupling was longer than the wavelength with the largest emission cross-section.[45,48,250]

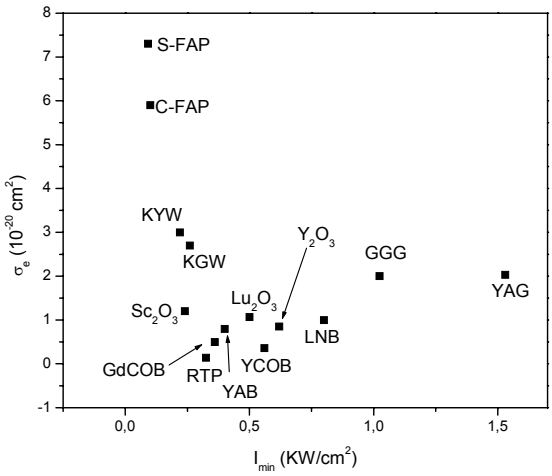

Figure 7.20. *Figure-of merit for RTP:(Nb,Yb) crystals and several promising Yb-doped hosts.*

As the favourable positions in this figure are for the low values of I_{min} and high values of σ_e, RTP:(Nb,Yb) crystals are not very bad situated in this figure and could be good promising crystals for lasing Yb^{3+}.

7.4. The Non-Linear Optical response of $RbTiOPO_4$:(Nb,Ln) crystals.

Figure 5 in *paper IX* shows the results from the study of the SHG efficiency of RTP:(Nb,Ln) (Ln = Er and Yb) crystals measured using the powder technique. Although the efficiency of these crystals is excellent, it seems that as the concentration of Ln^{3+} in the crystals increases, SHG efficiency decreases, and is clearly less than the SHG efficiency of an RTP crystal that contains only Nb at a similar concentration (see Chapter 6). However, efficiency did not drop dramatically at the level of dopants we studied. As we explained in *paper IX*, SHG efficiency depended strongly on the ratio between the concentrations of Nb and Ln. This lower SHG efficiency can be attributed to the fact that octahedral environment of TiO_6 in crystals containing Nb and lanthanide ions is more symmetrical than in crystals containing only Nb. For crystals containing Er^{3+}, we must consider an additional absorption of green light by this ion (see *papers III*, *VII* and *IX*).

We also determined the fundamental wavelengths of type II angular non-critical phase matching (NCPM) for second harmonic generation (SHG) for $RbTi_{0.967}Nb_{0.026}Er_{0.007}OPO_4$ and $RbTi_{0.93}Nb_{0.05}Yb_{0.02}OPO_4$ crystals. The λ_{NCPM} in the plane *y-z* represents the minimum value of the fundamental wavelength that can be doubled by the crystal. The results are shown in Table 7.6.

These wavelengths are lower than those of RTP (see Chapter 6) because of the Nb in the crystals, but they are not as low as those of $RbTi_{0.94}Nb_{0.06}OPO_4$. However, these wavelengths are not

only a function of the Nb content of the crystals. We must also take into account the concentration of Ln, which affects the NCPM wavelengths in the opposite way to the concentration of Nb.

Table 7.6. *Fundamental wavelengths for the angular non-critical phase-matching interactions in* $RbTi_{0.967}Nb_{0.026}Er_{0.007}OPO_4$ *and* $RbTi_{0.93}Nb_{0.05}Yb_{0.02}OPO_4$ *crystals in the x-z and y-z planes.*

	Fundamental wavelengths of NCPM interactions (nm)	
	x-z plane	*y-z* plane
$RbTi_{0.967}Nb_{0.026}Er_{0.007}OPO_4$	1111.4 ± 0.3	1006.2 ± 0.1
$RbTi_{0.935}Nb_{0.043}Yb_{0.022}OPO_4$	1114.7 ± 0.5	

Initial Page Table of Contents